Biaxial High Cycle Fatigue of a Type 304L Stainless Steel: Cyclic Strains and Crack Initiation Detection by Digital Image Correlation

M. Poncelet, G. Barbier, B. Raka, S. Courtin, R. Desmorat, J.C. Le-Roux, L. Vincent

Accepted Manuscript

Title: Biaxial High Cycle Fatigue of a Type 304L Stainless Steel: Cyclic Strains and Crack Initiation Detection by Digital Image Correlation

Authors: M. Poncelet, G. Barbier, B. Raka, S. Courtin, R. Desmorat, J.C. Le-Roux, L. Vincent

PII: S0997-7538(10)00068-9

DOI: 10.1016/j.euromechsol.2010.05.002

Reference: EJMSOL 2616

To appear in: *European Journal of Mechanics / A Solids*

Received Date: 8 February 2010

Revised Date: 16 April 2010

Accepted Date: 12 May 2010

Please cite this article as: Poncelet, M., Barbier, G., Raka, B., Courtin, S., Desmorat, R., Le-Roux, J.C., Vincent, L. Biaxial High Cycle Fatigue of a Type 304L Stainless Steel: Cyclic Strains and Crack Initiation Detection by Digital Image Correlation, European Journal of Mechanics / A Solids (2010), doi: 10.1016/j.euromechsol.2010.05.002

Biaxial High Cycle Fatigue of a Type 304L Stainless Steel: Cyclic Strains and Crack Initiation Detection by Digital Image Correlation

M.Poncelet[a1], G. Barbier[b], B. Raka[b], S. Courtin[c], R. Desmorat[b], J.C. Le-Roux[d], L. Vincent[a]

[a] CEA Saclay, DEN, SRMA, F-91191 Gif-sur-Yvette Cedex
martin.poncelet@cea.fr, ludovic.vincent@cea.fr

[b] LMT Cachan (ENS Cachan/CNRS/UPMC/PRES UniverSud Paris),
61 av. du Président Wilson, F-94230 Cachan
barbier@lmt.ens-cachan.fr, raka@lmt.ens-cachan.fr, desmorat@lmt.ens-cachan.fr

[c] AREVA NP SAS, Tour AREVA, F-92084 Paris La Défense
stephan.courtin@areva.com

[d] EDF - R & D, Département Matériaux et Mécanique des Composants
Avenue des Renardières - Ecuelles
F-77818 Moret Sur Loing Cedex
jean-christophe.le-roux@edf.fr

Abstract

A series of biaxial High Cycle Fatigue tests at room temperature is performed to build up an extensive and well-documented database. The testing specimen is a maltese cross thinned in its centre with non homogeneous strain/stress fields. The experimental protocol uses exclusively full-field strain measurements. The strains (cyclic and residual) as well as the crack initiation detection are obtained by use of Digital Image Correlation (DIC) techniques combined with a multiscale stroboscopic image acquisition *in situ* set-up. Nine cruciform specimens made of type 304L austenitic stainless steel are loaded by a multiaxial testing machine.

Two kinds of loading paths are presented: equibiaxial with a load ratio of 0.1, non-proportional with a cyclic load in one direction and a constant load in the other. The experimental results are given (strain amplitude, residual strain, number of cycles to crack initiation) for each loading path. The time history of local strain amplitudes and residual strains are recorded and plotted. Total strain vs. number of cycles fatigue curves show the different trends associated with each loading path. For instance, non-proportional loadings are found very damaging and leading to strong ratchetting effects.

The tested material is briefly introduced, followed by an in-depth description of the experimental set-up. The fatigue test campaign results are then presented, with a final discussion.

Keywords: Biaxial High Cycle Fatigue, crack initiation, Digital Image Correlation, stroboscopic image acquisition

* Corresponding author. tel : (+33) 1 69 08 68 72 / fax : (+33) 1 69 08 71 67

1 Introduction

Fatigue loading encountered in real structures may be complex, *i.e.* multiaxial and anisothermal with non-constant amplitude. Fatigue design tools for such cases are needed, in order to avoid early fatigue failure which may be dramatic.

An illustrating example is the following incident which happened in may 1998 on the Residual Heat Removal System (RHRS) of the French Civaux 1 nuclear power plant (1400 MWe N4 type Pressurized Water Reactor). This incident was classified as level 2 of the INES scale that includes 7 levels. It had in fact no impact on the environment (and there was no risk to people) and a modification of all RHRS circuits has been made since. The role of this pipes system is to evacuate the heat of the primary cooling system and the residual power of the fuel, and to maintain the primary coolant water at low temperature. In Civaux 1, a leak of primary liquid was detected in the RHRS which was then in the hot shutdown conditions (Faidy *et al.,* 2000) and inspections revealed a longitudinal crack in a weld joining two forged pipe sections in the by-pass piping of the RHRS heat exchanger. A network of micro-cracks was also identified. The RHRS circuit consisting in two redundant paths, the leak was stopped by isolating one of them.

The investigations for understanding the cracking mechanisms (Cipiere and Goltrant, 2002 ; Molinie, 2002 ; Stephan *et al.*, 2002) pointed out that the inner wall of the pipes is submitted to time temperature fluctuations coupled with spatial fluctuations in fluid mixing zones. This High Cycle Thermal Fatigue phenomenon occurs in pipes where flows at different temperature and different flow rate ratio mix in a turbulent manner. Local or global temperature fields resulting from this turbulent mixing lead to mainly biaxial and non periodic thermal stresses that may cause fatigue damage. The frequency of thermal fluctuations is a random spectrum, leading rapidly to the accumulation of a large number of cycles. To sum up, such a complex loading combines high frequency biaxial stresses fluctuations (with variable and low level amplitudes) with a biaxial mean stress due to constant pressure and permanent long range heterogeneity of temperature. This type of loading was already known as able to induce fatigue damage characterized by a network of micro-cracks and of deeper cracks along geometric singularities like welds (Faidy *et al.,* 2000), as in the Civaux 1 configuration, where the flow can be locally disturbed.

A complete analysis of such a complex fatigue case involves expertise in thermal hydraulics (for the pipe thermal loading induced by the fluid), thermo-mechanics (for the structure response calculation) and materials (for the multiaxial fatigue strength) (Chapuliot *et al.* 2005; Kimura *et al.*, 2007; Paffumi *et al.*, 2008). The temperature variations are not considered next (for design in the anisothermal cases refer for instance to (Charkaluk and Constantinescu, 2000; Chellapandi *et al.*, 2009; Desmorat *et al.*, 2007; Lemaitre *et al.*, 2009; Otin *et al.*, 2007; Sermage *et al.*, 2000)). One will focus on the mechanics and materials topics.

Many fatigue design laws are based on uniaxial characterization tests and transferability factors (Manson and Hirschberg, 1964). As Low Cycle Fatigue biaxial results are not numerous and as biaxial High Cycle Fatigue (HCF) tests are rare (see (Cognard *et al.*, 1997; Itoh *et al.*, 1994; McClaren and Terry, 1963; Pascoe and de Villiers, 1967; Wilson and White, 1971)), multiaxial fatigue design laws or models taking into account the mean stress effect (Barbier, 2009; Charkaluk and Constantinescu, 2000; Crossland, 1956; Dang Van, 1973; Dang Van and Papadopoulos, 1999; Desmorat *et al.*, 2007; Doudard *et al.*, 2007; Fatemi and Yang, 1998; Sines, 1959) miss experimental data to be fully validated.

In order to get results in conditions representative of the one encountered in pipes, one has chosen to take advantage of the LMT-Cachan triaxial machine performance to make a biaxial High Cycle Fatigue testing campaign on an AISI type 304L steel. This paper presents

two series of tests, namely an equibiaxial loading path with a loading ratio set to 0.1, and a non-proportional one with a constant load in one direction and a cyclic load in the perpendicular direction, also with a loading ratio set to 0.1. Another novelty is the use in High Cycle Fatigue (at 10 or 20 Hz) of Digital Image Correlation (DIC) (Hild and Roux, 2005). This allows for an accurate measurement of the local strains (at the centre of the biaxial specimen) under cyclic loading, and for the *in situ* observation of crack initiation thanks to a stroboscopic and multiscale optical measurement set-up.

2 Material data for type 304L steel

The material used in this study is an AISI type 304L austenitic stainless steels. It has been provided by Creusot Loire Industries (CLI) as a 30 mm thickness rolled sheet. It is therefore named "304L CLI". Its chemical composition and main mechanical characteristics presented hereafter fulfil the required conditions of the ASME (USA) and RCCM (France) design codes for Nuclear Reactors.

2.1 Main characteristics

The chemical composition (wt. %) of the 304L CLI is given in Table 1. Considering only the chemical composition, the start temperature under which martensitic transformation occurs is estimated below the absolute zero (Eichelmann and Hull, 1953; Faidy *et al.* 2000), namely martensitic transformation is not possible**.** However, at room temperature, some martensite can be created with the contribution of plastic deformation, especially in fatigue loadings (Kaleta and Zietek, 1998; Kurpp *et al.*, 2001; Müller-Bollenhagen *et al.*, 2010). As illustrated later, such a martensite transformation is considered as responsible for the secondary strain hardening of the material at room temperature (Colin *et al.*, 2010; Kaleta and Zietek, 1998).

Table 1: Chemical composition of studied type 304L Stainless Steel (%Wt), from (Akamatsu and Chevallier, 2001).

The grain size has been determined according to the French standard NF A 04-102 in the bulk and near the side of the sheet. The grain size is around 150 µm in rolling direction, and 125 µm in transverse direction. Microstructural heterogeneity is present and some lamellar ferrite is observed in the rolling direction.

Monotonic mechanical properties have been determined from tensile tests in rolling and transverse directions. From the experimental results reported in Table 2, the material can be considered as isotropic.

Table 2: Monotonic mechanical properties for the studied type 304L stainless steel, from (Akamatsu and Chevallier, 2001).

2.2 Uniaxial cyclic behaviour of the type 304L stainless steel

Uniaxial room temperature High Cycle Fatigue tests have been performed on different type 304L stainless steels including the one that will be tested in the biaxial apparatus. Strain controlled fatigue tests are usually recommended in design codes such as ASME or RCCM, but stress controlled tests have also been performed in order to check for any controlling variable effect on lifetime. Some tests have been performed at elevated temperature (Fissolo *et al.*, 2009), in different environments (Solomon *et al.*, 2004), and/or with different strain rates but these results are not reported here.

At room temperature, the mechanical behaviour of type 304L stainless steels in High Cycle Fatigue evolves during lifetime and for some loading conditions, a stabilized state is never reached. After a limited number of cycles during which classical strain hardening occurs, cyclic softening is observed during several thousands of cycles (as shown in Figure 1) and finally a secondary hardening can take place until the end of cycling or final failure depending on the material grade and on the test loading conditions.

Figure 1 : Stress amplitude as a function of the number of cycles. Evolution of the stress amplitude as a function of the number of cycles for two type 304L stainless steels (304L CLI and 304L THYSSEN) at room temperature (see (Le Roux, 2004)).

This particular evolution of cyclic behaviour is observed both in strain and stress controlled tests for a 304L grade for which secondary hardening is strong (304L THYSSEN grade) as reported in (Vincent and Perez, 2005).

The grade studied in this work (304L CLI) shows a secondary hardening less pronounced than for the 304L THYSSEN. The cyclic behaviours of both grades can be observed in Figure 1 which reports the stress amplitude as a function of the number of cycles for several controlled strain amplitudes (Le Roux, 2004). Results corresponding to 304L CLI and 304L THYSSEN are plotted respectively with filled squares (CLI) and crosses (THYSSEN).

Preliminary TEM observations suggest that secondary hardening at room temperature may be due to progressive martensite transformation (Renault, 2006). This result is in agreement with the differences in chemical composition of both grades as the start temperature of martensite transformation calculated from (Eichelmann and Hull, 1953) is 50°C higher for 304L THYSSEN than for 304L CLI. The average grain size of 304L THYSSEN is also smaller (~ 40μm) than the one of 304L CLI (~ 120μm) which is in favour of more martensitic transformation and of a longer lifetime for the THYSSEN alloy according to (Stolarz *et al.*, 2001).

Note that at elevated temperature (T>200°C), secondary hardening also occurs but this time, its origin is the development of a specific dislocation microstructure called corduroy. This microstructure is observed in materials with low stacking fault energy which plastically deform essentially by planar slips in low amplitude proportional fatigue tests (see a complete study in (Gerland *et al.*, 1997) concerning type 316L stainless steels).

Uniaxial fatigue curves are available for both strain controlled tests and stress controlled tests (Solomon *et al.*, 2004). Secondary hardening increases the fatigue strength of the material at least in terms of stress amplitude. As a matter of fact, after one million cycles reached with the endurance strain amplitude, the material can resist to cyclic stress amplitudes much larger than the endurance stress amplitude (~ 40% higher for 304L THYSSEN at half-lifetime from Figure 3). Consequently, it is important not to use strain (stress) controlled fatigue tests to identify stress (strain) endurance limits by taking half-lifetime value for instance, as it might lead to non conservative predictions. This benefit effect of secondary hardening on fatigue strength is also observed for type 316L stainless steels at 400°C (Gerland *et al.*, 1997).

Let us point out that classical methodologies to estimate critical stress and strain states in a structure submitted to fatigue loading use Finite Element computations in which the plasticity model is rather rough and cannot properly describe the complete type 304L complex evolution of material behaviour during the whole loading. Besides, computing all cycles is not suitable in an engineering design and is still out of hand in structural fatigue. Only a few cycles are effectively computed, or a “jump in cycle” method is necessary to take into account

material cyclic behaviour evolution (Chaboche and Lesne, 1988; Lemaitre and Doghri, 1994). Therefore, the choice for the equivalent mechanical behaviour of the material over these few cycles is an open question when no stabilized hysteresis loop can be experimentally obtained.

Last, material ratchetting occurs in the presence of mean stress. This phenomenon has been intensively investigated both experimentally and theoretically since the 1980's (Bari and Hassan, 2000; Chaboche, 1991; Delobelle *et al.*, 1995; Ohno and Wang, 1993; Portier *et al.*, 2000). The nuclear industry has lead many studies in this field and uniaxial experimental results are available on type 316L stainless steel (Bocher *et al.*, 2001; Delobelle *et al.*, 1995; Portier *et al.*, 2000). Concerning fatigue life, in the presence of a limited mean stress of less than 50 MPa, stress endurance limit is slightly modified (Colin *et al.*, 2010; Vincent and Perez, 2005). On the contrary, the same mean stress induces a large decrease (~ 30%) of strain endurance limit (Vincent and Perez, 2005). Unfortunately the study of the influence of a mean stress on the fatigue curves, uniaxial or biaxial, requires a large amount of experimental results. This task still has to be completed for type 304L stainless steel.

3 Experimental set-up for biaxial fatigue

To the authors' knowledge, the experiments described herein are original because they are at the intersection of several previous experimental investigations. For control simplicity and cost, most of the multiaxial fatigue tests are performed using "one-axis testing machines": the early bending torsion tests (Lanza, 1886; Mason, 1917), then the tension-torsion and tension-internal pressure tests (Marin, 1949) or even more recent tension-torsion-internal pressure tests (Andrew and Ellison, 1973; Lefebvre *et al.*, 1983). Very few are conducted on "two axis" (*i.e.* bitension) machines for they are rare and more complex (Cognard et al., 1997; Itoh et al., 1994; McClaren and Terry, 1963; Pascoe and de Villiers, 1967; Wilson and White, 1971). They however allow a wide range of loading paths, without any protocol change (especially no specimen geometry modification), which is an important parameter in the case of a fatigue campaign. For instance, different biaxial fatigue and creep-fatigue test at high temperature in non-proportional (and anisothermal) conditions where performed on the same specimen geometry thanks to the multiaxial machine presented hereafter (Sermage *et al.*, 2000). Moreover, most of the biaxial tests are limited to the low cycles fatigue regime because of their duration (some reach nonetheless 10^6 cycles, *e.g.* (Bedkowski, 1994; Bonnand *et al.*, 2009)). On top of that, materials presenting plastic strains in the High Cycles Fatigue regime, such as type 304L stainless steel, are hardly ever tested in multiaxial HCF since the local stresses and/or strains amplitudes are more difficult to control during the whole test.

3.1 ASTREE triaxial testing machine

The triaxial testing machine ASTREE (Calloch and Marquis, 1999) of the LMT-Cachan laboratory is used. Several tests with cyclic loadings have already been performed on cross specimens with this machine (Bedkowski, 1994; Doudard *et al.*, 2007; Sermage, 1998; Sermage *et al.*, 2000): they are similar to Low Cycles or High Cycles Fatigue tests in terms of strain amplitudes, nonetheless the applied number of cycles is always below 10^5.

The loading frame of the machine is composed of a fixed base, four vertical columns and a mobile crosshead. Among the six available servohydraulic actuators, the four horizontal ones are used for the tests. They have a load capacity of 100 kN and a 250 mm stroke range. They are freely and independently relocated along the vertical columns. For protection against potential side and twist forces applied by other actuators, an additional hydraulic bearing is installed in front of each actuator. The hydraulic power is supplied by stations that can generate a 660 L/min maximum flow rate.

The testing machine is commanded by a highly versatile digital controller (Instron 8800) and by its related interface software (Consol 8.2 build 133). This allows for each actuator to be controlled independently, but also to perform virtually any closed-loop control using linear combinations of the different input signals. In the case of the biaxial tests presented hereafter, a special control type inspired by (Shiratori and Ikegami, 1967) called "modal control" is used. It is based on a relationship between the two forces F_1 and F_2 of two opposite actuators along the same load axis (X,Y or Z) to control both the mean force $(F_1 + F_2)/2$ and the force difference $(F_1 - F_2)/2$. Consequently the loading is "balanced" between the two actuators if the imposed force difference is zero, and the centre of the specimen is maintained motionless. The digital controller enforces modal control by using special algorithms to operate the valve driver of each actuator.

The main reason for force-controlled tests is that at the beginning of this study, tension-compression loadings have not been considered since buckling may occur, *i.e.* only tests with a positive loading ratio have been performed. In this case, force-controlled tests must be performed because the cyclic relaxation due to plasticity may lead to compressive stress in displacement-control.

3.2 Thinned maltese cross shaped specimen

The testing specimen has to be designed in order to allow for crack initiation in biaxial conditions, *i.e.* at the centre of a cruciform specimen loaded in ASTREE machine. Consistently, the design of a maltese cross shaped specimen already tested in this machine (Sermage *et al.*, 2000) has been improved following a two stages procedure:

- first, elastic computations are performed so that the von Mises stress σ_{eq} and the damage equivalent stress σ^* (Lemaitre, 1992)

$$\sigma^* = \sigma_{eq} R_\nu^{1/2} \quad \text{and} \quad R_\nu = \frac{2}{3}(1+\nu) + 3(1-2\nu)\left(\frac{\sigma_H}{\sigma_{eq}}\right)^2 \tag{1}$$

  are higher in the specimen centre than in notches between arms. The advantage of considering σ^* criterion is that stress triaxiality (biaxiality here) $\sigma_H/\sigma_{eq} = \frac{1}{3}\sigma_{kk}/\sigma_{eq}$ is taken into account in the design;
- second, the theoretical location of the first crack initiated is checked from damage post-processing of the elastic computations (using the two scale damage model (Desmorat *et al.*, 2007; Lemaitre and Doghri, 1994; Lemaitre *et al.*, 1999) detailed in Appendix A, implemented in DAMAGE_2005 thermo-mechanical fatigue code (Desmorat *et al.*, 2006)).

Doing so, one ends up with the optimized geometry presented in Figure 2. The thickness at the centre is equal to 1 mm, increasing to 5 mm out of the gauge zone. The notches radius is 12 mm. The ratio between the number of cycles to crack initiation in the notch free edge N_i^{notch} and in the centre N_i^{centre} is calculated with DAMAGE_2005 for different loading paths. The average ratio is 2.3, *i.e.* $N_i^{centre} < N_i^{notch}$ as expected. Such a factor is not large compared to usual fatigue discrepancy, so that the notches angles have been rounded to prevent microcracks due to machining in these areas to propagate toward the centre (see cross section BB in Figure 2). The measured roughness on the centre of the gauge zone is R_a ~ 1.1 (R_t ~ 8.7), which is representative of certain in-service component areas roughness.

Figure 2 : Optimized testing specimen geometry.

Note that the thinned maltese cross specimen, originally designed for positive load ratios, has proved able to support symmetric biaxial fatigue loading. This will allow to complete the present campaign with equibiaxial tests at load ratio *R=-1*.

3.3 Additional measurement devices

Because of the not so well known multiaxial cyclic behaviour of the material and of the complex geometry of the specimen, it is almost impossible to calculate accurately the stress and strain state in the specimen thinned (gauge) zone. It is thus necessary to quantify experimentally the strain in the centre of this zone during the test. Moreover in the present study one wants to observe where crack initiation occurs.

This double goal is achieved through a compound (parallel) measurement of the strain field by Digital Image Correlation (DIC) based on the complementary acquisitions of two cameras (Figure 3): a high resolution Digital Single Lens Reflex (DSLR) camera is dedicated to the inspection of the whole gauge zone while a digital high performance camera with a high magnification lens allows accurate strain measurement in the specimen centre. The second is a CCD camera with a telecentric lens. Both are on the same side of the specimen and share the same optical axis thanks to an optical set-up based on a beam-splitter.

Figure 3 : Experimental protocol.
(a) optical set-up ; (b) DSLR frame (the rectangle symbolises the CCD frame) ; (c) CCD camera frame. The two strings visible on (b) and (c) are used to target the centre of the gauge zone before the test.

Figure 4 : Chronological organisation of a test. Scheme of the chronological organisation of a typical test using stroboscopic effect. In this example, *n = 8* and *N = 2* (*t* : time; *F* : mean load; *stars* : triggering time for *DSLR* camera or *CCD* camera).

The controller of ASTREE machine stops the cyclic loading periodically (usually after every series of 5×10^3, 10×10^3 or 20×10^3 cycles) to acquire images from the whole gauge zone at maximum and zero load (Figure 4) with the DSLR camera. Images are recorded on a dedicated computer. A Digital Image Correlation software (CorreliQ4, (Besnard *et al.*, 2006)) is then used to obtain the strain field in the whole gauge zone. When the DIC is performed between images at maximum load, it leads to an insight of the evolution of the cyclic behaviour of the whole structure (the obtained strain field would be constant if no evolution of the cyclic behaviour occurs) and to the detection of cracks (see also (Rupil *et al.*, 2009), or for the use of DIC for crack Stress Intensity Factor measurement see for example (Hamam *et al.*, 2007; McNeill *et al.*, 1987)). The accurate date and location of crack initiation are thus measured for each test. When the DIC is performed between images at zero load, it measures the residual strain map in the gauge zone.

Contrary to DSLR cameras, digital cameras (*i.e.* without mechanical parts) have virtually no shutter lag, so that acquisition under cyclic loadings with continuous lighting is possible. The digital camera is thus *not* triggered synchronously with the DSLR camera (Figure 4). A sub-sampling stroboscopic method is chosen to use this standard camera instead of an expensive high speed camera. It fits fatigue tests provided it is solely applied to cyclic phenomenon. To the authors' knowledge, this method has not been used for Digital Image Correlation until recently (Vanlanduit *et al.*, 2009). It consists in acquiring images with a period τ_{acq} longer than the load period τ_l, in such a way that

$$\tau_{acq} = \tau_l \left(N + \frac{1}{n} \right). \quad (2)$$

where N and n are positive integers. N is chosen so that $\tau_l N > \tau_l^{\min i}$, the minimum period enabled by the acquisition system. The integer n is the sampling step and the total number of recorded images. If equation (2) is satisfied, the sequence of images represents a complete load cycle. In the present case, the experimental protocol is however different from the one proposed in (Vanlanduit *et al.*, 2009). First, the actual frequency of the loading is measured through the load cell signal before each sequence recording. Second, the period of acquisition is calculated, and the *camera* (and not a flash light) is triggered for each image. In the present case the integer N is set to 10 and the integer n is set to 20 to have a reasonably accurate description of a whole cycle after the realization of 200 real cycles

The sub-sampling system is in stand-by mode during most of the test duration. A sequence of n images is only recorded at the beginning of every load sequence, *i.e.* every 5×10^3, 10×10^3 or 20×10^3 cycles (Figure 4). A dedicated computer and a Labview (NI, 1999) routine are used to implement the sub-sampling method, triggered by the digital controller of the testing machine, and triggering the camera. Images are directly recorded on the computer. The Digital Image Correlation is performed on each sequence. The reference image is taken at the beginning of the test, before any loading, so that DIC gives for each sequence the absolute strain. An "optical strain gage" function is performed on an area of 3×3 mm^2 located in the centre of the gauge zone in order to compute the spatial average of the strain value over this area. Last a sine function is fitted on the strain cycle with the least square method to measure the strain amplitude and mean strain. The mean strain is also measured on a larger area with the Digital Single Lens Reflex camera after each loading sequence.

Two different optical devices are placed on the other side of the specimen, depending on the test. No beam-splitter system is needed because only one optical set-up is used at a time. For some of the tests, a second sub-sampling set-up is rigged up to measure simultaneously the strain in the centre of the gauge zone of this side. It is composed of an other set of digital camera) and a telecentrique lens, triggered simultaneously with the afore-mentioned digital camera. Data processing is exactly the same as for the sub-sampling on the opposite side. For the other tests, a microscopy set-up is in place of the sub-sampling one. The gauge zone is not covered by a painted speckle to see directly the as-milled surface. It allows for the observation of crack initiation and propagation and a better understanding of the influence of the striae left over from the milling process on cracks behaviour. Figure 5 presents an *in-situ* view of this set-up, composed of a DLSR camera mounted on a Long Distance Microscope. The frame is about 2×2 mm². An example of the recorded micrograph is shown in the upper left corner of Figure 5. The very short field depth (< 30 μm) does not allow to acquire pictures at zero and maximal load (because of small but non-zero out-of-plane displacement), nor during the cyclic loading (small vibration). Only pictures at zero load are shot.

For complementary details on the whole measurement set-up, refer to Appendix B.

Figure 5 : Microscopy set-up. ([a] Digital Single Lens Reflex or DSLR, [b] Long Distance Microscope, [c] Diffuse lighting, [d] cross-specimen, [e] beam-splitter set-up). In the upper left corner, an example of *in-situ* micrograph taken by the Long Distance Microscope (note that the lighting is chosen to enhance the machining striae visibility).

3.4 Validation of boundary conditions - Strain field measurements

The tests conditions have to be validated prior to any test. As it will be shown in the following section 3.4.1, the strains characteristics (biaxiality and load ratio) in the specimen centre may differ from the applied forces despite the great care during the machine adjustment and the specimen clamping. This feature justifies all the more the need for extensive *in-situ* strain measurements, which capacities are assessed in sections 3.4.2 and 3.4.3.

3.4.1 Loading

The correct application of the mechanical loading must be checked, from the clamping of the specimen to the fatigue test itself. A specimen is equipped with a miniature three-element 60° delta rosette (Vishay, 015YD) on each face, in the centre of the gauge zone. When the actuators are not correctly positioned, an important bending strain or rotation may be observed during the clamping and loading of such cross-specimens (Bouvet *et al.*, 2002; Doudard *et al.*, 2007). When an accurate positioning of the actuators is obtained, the strains due to clamping are of the order of 10^{-4} *i.e.* no plasticity is induced and the corresponding stress level is about 20 MPa.

Three different equibiaxial loading paths are then performed on this specimen: three with a load ratio $R_F = F_{\min}/F_{\max} = -1$ and a maximum force $F_{\max} = \{19\,\text{kN}, 21\,\text{kN}\}$, and one with $R_F = 0.1$ and $F_{\max} = 28\,\text{kN}$. Each of them lasts 1000 cycles at 10 Hz. Those loading conditions are chosen to represent typical loadings and minimize the risk of strain gauge debonding due to large values of permanent strains. The forces applied by the machine are measured to assess the quality of the closed-loop control in real conditions. The same features are revealed by the four measurements, so that only the test at 21 kN is presented for the sake of brevity. Figure 6 shows that the loading ratio as well as the equibiaxiality are respected in terms of applied forces. The difference between forces on the same load axis is less than 2.5 % of the maximum force. The temperature of the gauge zone is also checked by infrared thermography. It does not exceed 50°C whereas the actuators' temperature is about 40°C in regular conditions.

The strain rosettes signals are also recorded during these tests. Once more, only the results for 21 kN are presented. The variation of the angle between the directions of eigenstrains and the specimen coordinate system is negligible and the test is thus considered as proportional. The variations of eigenstrains on both faces of the specimen are shown in Figure 6b. Despite a good agreement between strain loading path and force loading path at first sight, several points are worth noting. First, the local strain loading ratio $R_\varepsilon = \varepsilon_{\min}/\varepsilon_{\max}$ at the specimen centre is not equal to –1. Depending on the considered direction and face of the specimen, values range from -0.55 to -1.73. This fact is not surprising, since the non-zero mean strains are direct consequences of the clamping static bending. Even though these mean strains do not vanish over cycles, one may suppose that mean stresses tend to zero because of a cyclic relaxation phenomenon. Second, a non-negligible difference (< 14 %) of strain amplitude appears between the two faces and the two directions. It denotes bending in spite of the careful positioning. These divergences between applied forces and actual strains in the centre of the gauge justify all the more the optical strain measurements during cyclic loading. The validation of these measurements is presented in the following section.

Figure 6 : Forces and strain gauges measurement for an equibiaxial test ($R_F = 0.1$, $F_{\max} = 21\,\text{kN}$, N=1000 cycles). (a) Mean force along loading axis 1 versus mean force along loading axis 2. (b) First eigenstrain ε_I versus second eigenstrain ε_{II} for both faces of the gauge zone.

3.4.2 Optical DIC strain gauge

A loading at low frequency (0.055Hz) is performed so that both Digital Single Lens Reflex and digital camera are able to acquire images during cycling. The strain is then calculated on the same 3 x 3 mm^2 area for both cameras. The results are presented in Figure 7 (consequently this figure does not represent an "as-performed" loading since DSLR could not be enough accurately triggered for a 10Hz test). Besides allowing for acquisition at high frequency, the digital camera and its close-up enable far lower uncertainties. To assess the measurement uncertainty accurately, twenty images are shot in the test conditions, but with the load amplitude set to zero. The standard deviation of the computed strain signal is below 2×10^{-5} for each in-plane component ε_{11}, ε_{22} and ε_{12}. The strain amplitudes obtained by optical measurement are compared to strain gauge results for the four previously presented loading paths. These results correspond to two different specimens (since the strain gauge set-up disables Digital Image Correlation). Both measures are performed after the same number of cycles. The difference of amplitude is in any case below 5×10^{-5}, much lower than the typical amplitudes of the following fatigue tests (about 10^{-3}). The stroboscopic Digital Image Correlation measurement method is thus validated.

Figure 7 : Measurement of strain cycles. Comparison of the strain cycles measured by the digital single lens reflex with macro lens (DSLR) and the digital camera with telecentric lens (DC).

3.4.3 Strain field measurement and DIC-based crack initiation observation

Since the initiation of a crack leads to a brutal increase of the strain, the Digital Image Correlation software (CorreliQ4 (Besnard *et al.*, 2006)) is used for an *a posteriori* determination of the number of cycles to crack initiation N_i and not to rely on the number of cycle to failure (which depends on the crack propagation time). This type of analysis is performed only on the lower side of the specimen since it uses the DSLR which is only available on this side in the present experimental set-up. As shown in

Figure 8b for an equibiaxial test, a millimetric crack is clearly detectable during a test when the DIC is performed between a pair of images of the Digital Single Lens Reflex at maximum load (or a pair at zero load), whereas it cannot be seen with the naked eyes at the same number of cycles (

Figure 8a). Once the crack initiation location is found, the DIC is performed with 16 x 16 pixels Zone Of Interest (ZOI, *c.a.* 0.65 x 0.65 mm^2) on the previous images in order to find the first appearance of the crack. This technique allows for detecting cracks as small as one ZOI size in the best case (in most of the cases the crack that was undetectable on a previous image has propagated to a length longer than the ZOI size, for examples see Table 4 and 5). Of course, as one does not have images for all the cycles of the test, one only knows during which series of 5 000, 10 000 or 20 000 cycles initiation occurs. Compared to the typical number of cycles to crack initiation, this uncertainty is considered as negligible.

This method is equivalent to a criterion of an average relative strain rate set to 5 % per 10 000 cycles over a 1 x 1 mm^2 area around the crack (this area is different from the previous 3 x 3 mm^2 area used for cyclic strain measurement in the absence of crack). As an example, Figure 9 presents the average strain of the initiation area as a function of number of cycles for the test corresponding to

Figure 8. A typical curve is obtained for this material: a first rapid increase of strain (up to few percents), a stabilisation and last the initiation with the sudden increase of the strain. The 5 % / 10 000 cycles criterion leads to a number of cycles to crack initiation of 83 000 cycles, which corresponds to the number of cycles of

Figure 8. One sees in Figure 9 that results obtained with images at zero load (residual strain) and maximum load (residual strain and total strain due to applied forces and crack opening) lead to the same number of cycles to crack initiation.

A second interest of this DIC-based crack initiation observation is that it allows for knowing accurately where the crack initiates and consequently whether a test is or is not validated (*i.e.* if the initiation occurs or not in the centre of the gauge zone). If the fracture area is not damaged during failure, a micrographic study can *a posteriori* give this piece of information (and additional ones) more accurately. However the present method has the advantage of being almost instantaneous. Last, it helps to understand step-by-step the scenario of initiation-propagation, *e.g.* to know if a first crack is responsible for the initiation of a second one or if both cracks were initiated almost independently. A final macroscopic crack can be formed by the coalescence of two or more smaller cracks and this scenario can be observed easily by Digital Image Correlation.

Figure 8 : Early crack initiation detection by DIC (equibiaxial test Fmax = 38 kN with R_F = 0.1). (a) gauge zone after 83 000 cycles. (b) : strain field after 83 000 cycles ; (c) gauge zone after 93 000 cycles.

Figure 9 : Evolution of strain in the crack initiation zone. Average strain over a 1 x 1 mm^2 area located at the crack initiation zone for the same test as in Figure 8. The 5 % per 10 000 cycles strain rate criterion leads to a number of cycles to crack initiation equal to 83 000 for images at zero load as well as for images at maximum load.

4 Biaxial fatigue campaign and results

This biaxial fatigue campaign presents several interests: two different loading types were performed until now, on a highly inelastic material in the HCF regime, up to 10^6 cycles, with DIC strains measurements and crack initiation detection. The *in situ* measurement of the strains during testing allows for biaxial $\Delta\varepsilon$–N fatigue curves as well as structure cyclic behaviour to be plotted. Post-mortem analyses enable complementary data.

4.1 Different loadings considered

Table 3 presents the loading types considered. The first and second groups respectively correspond to an equibiaxial $R_F = F_{min}/F_{Max} = 0.1$ loading path (ETT) and a non-proportional loading path (NP) with a cyclic loading along direction 1 and a constant loading along direction 2. All tests are stopped after 10^6 cycles unless failure has occurred before. All the crack initiations of the presented tests are located in the centre of the gauge zone.

Table 3: Definition of the loading paths.

4.2 Tests results

The different test results are gathered in Tables 4 and 5 depending on the type of loading. For each test, the main measured load characteristics are presented (*i.e.* maximum force F^{max} and load ratio $R_F = F_{min}/F_{Max}$ for each axis), as well as the strain amplitude $\Delta\varepsilon/2$ at half-lifetime and the residual strain $\varepsilon_{res}(N_i)$ at the number of cycles to crack initiation. One will see in next section that the variation of amplitude with the number of cycles is low except during the first 10^4 cycles, so that for most of the specimens the strain amplitude at half-lifetime is a meaningful characteristic of the performed test. The shear strain amplitudes are not presented in the tables because they are negligible before crack initiation (their magnitude is always less than 5 % of the tension strains and in most of the case less than 1 % so that their level is equivalent to the measurement uncertainty). The number of cycles to crack initiation N_i is given within a range equal to the last series of cycles duration, i.e. initiation is not yet detected at the lower bound and detected at the upper bound. In most of the tests, the duration of a series is set to 5 000 cycles (in some cases it is equal to 3 000 or 10 000). If the test is stopped without any crack initiation, the total number of cycles applied during the test is given. Furthermore, a strain field is presented for each test. This strain field is calculated using the image at vanishing load at N_i cycles, and the image at vanishing load of the previous series as the reference image. The presented strain field is thus equal to the increment of residual strains between the last two series of the test. The crack initiation is more easily detected with this type of plotting since the strain heterogeneity due to the crack is not lost in the residual strain due to the whole loading cycles. For the sake of clarity the same scale is used for every strain field.

Three non-proportional tension-tension tests were performed, with constant load ratio in one direction and constant load in the other direction (Table 4). Both applied loads and measured strains are reliable. The only reservation is the accuracy of the number of cycles to crack initiation N_i for NP2 and NP3 tests. Because of the duration of the series between each image acquisition for crack initiation detection (ΔN = 10 000 cycles in the case of NP2 and NP3 at the time of initiation) and the early initiation (N_i = 30 000 – 40 000 for NP2 and 45 000 – 55 000 for NP3) the accuracy is $\Delta N / N_i$ = 33 % for NP2 and 22 % for NP3. The substantial residual strains have to be noticed, so their opposite signs. The ratio of the strain amplitude along each axis is about 2 and the smaller amplitude is always along the axis of constant load. The strain amplitudes given in Table 4 are all positive by definition, but strain variations along both axes are in phase opposition for the three tests.

Six equibiaxial tests at load ratio $R_F = 0.1$ were performed (Table 5). They were the first to be conducted, and several technical problems prevent a complete characterization of some of them (ETT2(1), ETT3(1)). These tests were thus repeated later on (ETT2(2), ETT3(0), ETT3(2)) and the new strain amplitude measures are supposed to be similar to the previous ones, so that they are given in place of the missing values of previous tests (see comments in Table 5). In spite of the relatively good balance of the applied load, the strains (especially the residual strains) are not exactly equal because of the previously mentioned minor clamping and bending asymmetry. The influence of the surface finish seems low since micrographs show no clear link between crack orientation and machining striae. Last, the measurement of the number of cycles to crack initiation N_i are considered as accurate: the wider range of the numbers of cycles to crack initiation N_i is less than 10 % of the value of N_i (ETT3(0)).

To gather the different loading paths on a same fatigue curve, one proposes to present these results as total strain vs. number of cycles curves.

Table 4: Non-Proportional Tension-Tension with constant load tests results. The strain field shows the increment of residual strain during the last series of cycles, in the meniscus of the gauge zone. Depending on the crack orientation, ε_{xx} or ε_{yy} is plotted to better visualization. The circle stands for the gauge zone limit. The strain scale is the same for every test and the gauge diameter (black circle) is 30mm.

Table 5: Equibiaxial Tension-Tension (ETT) tests results.

4.3 Biaxial Fatigue curves

A scalar (therefore equivalent) strain amplitude has to be chosen to plot a Δε-N graph that gathers all the tests performed with different multiaxial loading types. One simply chooses next the "maximum principal strain amplitude" over a cycle calculated as follows:

$$\Delta\varepsilon_{\max} = \max(\Delta\varepsilon_{11}, \Delta\varepsilon_{22}, \Delta\varepsilon_{33}). \tag{3}$$

where $\Delta\varepsilon = \max(\varepsilon) - \min(\varepsilon)$ is the variation of the quantity, *i.e.* twice its amplitude.

The actual material behaviour stands between a purely elastic one and a purely plastic one, so that the value of the equivalent strain amplitude is included in these bounds. *In the case of pure elasticity* and plane stress ($\Delta\sigma_{33} = 0$), one has

$$\varepsilon_{33} = -\frac{\nu}{E}(\sigma_{11} + \sigma_{22}) \quad \text{and} \quad \sigma_{11} + \sigma_{22} = \frac{E}{1-\nu}(\varepsilon_{11} + \varepsilon_{22}). \tag{4}$$

where ν and E are the Poisson ratio and the elasticity modulus. The strain along the out-of-plane direction is thus given by

$$\varepsilon_{33} = -(\varepsilon_{11} + \varepsilon_{22})\frac{\nu}{1-\nu}. \tag{5}$$

and thus the maximum strain reads:

$$\varepsilon_{\max} = \max(\varepsilon_{11}, \varepsilon_{22}, -(\varepsilon_{11} + \varepsilon_{22})\frac{\nu}{1-\nu}), \tag{6}$$

In the fully plastic case, one has directly

$$\varepsilon_{\max} = \max(\varepsilon_{11}, \varepsilon_{22}, -(\varepsilon_{11} + \varepsilon_{22})) \tag{7}$$

because of the incompressibility assumption. Last the calculations of strain amplitudes from equations (6) and (7) are trivial since ε_{11} and ε_{22} strains are in phase for all the tests. Non-proportional tests with a constant lateral load are not *stricto sensu* in phase but in phase opposition, however amplitudes are also directly obtained provided that one takes care of the opposed sign between ε_{11} and ε_{22} strains. The maximum strain variation is in the general case

$$\Delta\varepsilon_{\max} = \max\left(\Delta\varepsilon_{11}, \Delta\varepsilon_{22}, \left|\Delta\varepsilon_{11} + \chi\Delta\varepsilon_{22}\right|\frac{\nu^*}{1-\nu^*}\right), \tag{8}$$

where $\chi = sign(\varepsilon_{11}.\varepsilon_{22})$ and where $\nu^* = \nu$ for elasticity and $\nu^* = 0.5$ for plasticity. The amount of plastic deformation has thus a tremendous influence on the maximum equivalent strain value for equibiaxial loading, which ranges from $1/2\max(\Delta\varepsilon_{11}, \Delta\varepsilon_{22}, 0.428(\Delta\varepsilon_{11} + \chi\Delta\varepsilon_{22}))$ (pure elasticity case with $\nu = 0.3$) to $1/2\max(\Delta\varepsilon_{11}, \Delta\varepsilon_{22}, (\Delta\varepsilon_{11} + \chi\Delta\varepsilon_{22}))$ (pure plasticity). In the latter case, the value is nearly twice the in-plane strains (exactly twice for perfect equibiaxiality).

The values corresponding to the pure elasticity assumption correspond to the maximum of the in-plane strain amplitudes for both equibiaxial and non-proportional loadings. Consequently the experimental results plotted in this way (considering lower bounds only) are similar to the "raw" results, *i.e.* simply using the in-plane amplitudes given in Table 4 and 5.

The total strain vs. number of cycles curves are plotted in Figure 10. The range of the equivalent strain amplitude value is symbolized by plotting the lower and upper bounds linked by a solid line for each test (similar to a discrepancy line). The plotted equivalent strain amplitude corresponds to cyclic behaviour at half-lifetime.

Figure 10: Fatigue curves. Total strain vs. number of cycles to crack initiation curves plotted with maximum equivalent strain amplitudes. The solid line curve stands for the uniaxial fatigue curve.

Previous uniaxial results (Le Roux, 2004) are also mentioned in these figures. They correspond to strain controlled tests with a load ratio equal to –1. These uniaxial tests are plotted to remind us of the "standard" uniaxial fatigue curve of type 304L steel. The accurate positions of the biaxial results with respect to the presented uniaxial ones cannot be discussed here since the uniaxial tests were performed on conventional tensile specimens with an area of the gauge zone different from the one of biaxial specimens. To compensate for this difference of gauge zone area on the mean fatigue results, one has to take into account the probabilistic aspect of fatigue phenomenon, especially in the endurance domain. However in the present case one has too little information to accurately correct this effect, so that uniaxial results are plotted as such. A rough estimation of the correction factor performed as in (Weibull, 1951), based on a Weibull distribution of strain values at endurance, leads to multiply uniaxial strain amplitudes by about 1.2 in order to be compared to the present biaxial results.

It is worth noting that the numbers of cycles to crack initiation given for uniaxial tests correspond to the detection of a 25 % final decrease of the stabilised stress range. This means that both criteria are based on a change in the cyclic behaviour, but uniaxial criterion is global contrary to the present biaxial one that is local (sudden evolution of the strain at the crack initiation point). However, typical crack sizes at initiation in uniaxial tests are comparable to the ones obtained in the present study.

Note last that the general trend observed in Figure 10 slightly depends on the chosen expression for the equivalent strain. For instance the same trend – *i.e.* position of biaxial points compared to uniaxial ones - is observed if von Mises equivalent strain is used (with slightly smaller strain amplitudes in case of equibiaxial loadings, and with slightly larger ones in case of uniaxial and non-proportional loadings).

4.4 Cyclic and hysteretic behaviour

Because of the evolution of the behaviour under cyclic loadings, a sole fatigue curve is a partial report of the performed tests. To complete this description, let us exploit the data collected by the sub-sampling set-up. The evolutions of the strain amplitude and of the residual strain at the centre of the gauge zone (3×3 mm^2 area) are presented in this section.

Figure 11 presents the same evolutions for the Equibiaxial Tension-Tension tests at positive load ratio $R_F = 0.1$. Contrary to the others tests, the residual strains for test ETT3(1) and ETT3(2) turn out to be noticeably not alike despite the same load amplitude. Moreover the strains along directions 1 and 2 are different. These tests were the first ones of the whole campaign, and the experimental protocol was not yet completely stabilised. Some clamping problems have appeared that were solved in the following tests (explaining the distinction

between the strains in the two directions at the very beginning of these two tests). The *in-situ* measurements however allow to know the real loading and to take it into account in eventual computations. Significant residual strains values (Figure 11a) are reached for ETT2 and ETT3 tests (about 4 to 8 % before initiation). The increase of residual strains is in good agreement with the number of cycles to failure for all the tests. The strain amplitude (Figure 11b) is nearly constant after an increase (*c.a.* +20 %) during the first 5×10^3 cycles for ETT2 (2) test.

Figure 11 : (a) : Evolution of the strains during the equibiaxial R_F=0.1 tests. (a) evolution of the residual strains with the number of cycles; (b) evolution of the strain amplitude with the number of cycles for ETT2(2) test.

Figure 12 shows the strains evolution for the Non-Proportional tests. The magnitude of the residual strains (Figure 12a) is important (until *c.a.* 17 %). The residual strains evolution is very different for each of the three tests. NP1 (zero constant lateral load) is characterized by a non-negligible positive ratchetting effect in the cyclic load direction and a negative one in the other direction, whose level is twice smaller. NP2 (constant lateral load equal to half the maximum cyclic load) has a positive ratchetting effect in the cyclic load direction three times smaller than for NP1, and virtually none in the other direction. Last, NP3 (constant lateral load equal to maximum cyclic load) presents a positive ratchetting effect in the direction of the constant load and no residual strains in the other. NP2 and NP3 have nearly the same number of cycles to crack initiation (resp. 5×10^4 and 6×10^4) despite important differences of residual strains evolution. Figure 12b shows the evolution of the strain amplitudes with the number of cycles. The amplitudes are nearly constant for NP1 test, with strain levels in good agreement with incompressibility and uniaxial stress state assumptions (*i.e.* the amplitude in the cyclic load direction is twice the amplitude measured in the direction of zero constant load). The two other tests present higher amplitudes in both directions.

Figure 12 : Evolution of the strains during the non-proportional tests. (a) evolution of the residual strains with the number of cycles; (b) evolution of the strain amplitude with the number of cycles.

5 Discussion on fatigue results

There is usually a major difficulty in the interpretation of non homogeneous field tests. Moreover, the present biaxial testing specimens are structures made of a material characterized by a complex cyclic behaviour evolution. These tests are force-controlled, so that they cannot be interpreted in terms of stress-controlled nor strain-controlled tests (any test reveals variations of the strain amplitude, see Figure 11b and Figure 12b). One has to keep in mind this feature while comparing them with more conventional (uniaxial) fatigue tests.

The tests performed until now only allow for comparing proportional and non-proportional loadings with the same loading ratio (R_F=*0.1*).

As expected, biaxial ratchetting takes place for both loading types with R_F=*0.1* and leads to important residual strains in the centre of the gauge zone. Due to structural effects, an explanation could have been that a cyclic relaxation occurs in this region and that the main part of the mean stresses is then be redistributed in the surrounding elastic region. This explanation turns out to be wrong to some extent since the ratchetting effect longs up to failure. It is also worth noting that the Non-Proportional tests present even more important

residual strains due to ratchetting effect by comparison with the proportional test ETT3 which has the same force amplitude (17.1 kN).

An apparent detrimental effect of the non-proportionality is observed on fatigue life. Non-Proportional tests NP2 and NP3 (with a non-zero constant lateral load) have an equivalent strain amplitude smaller or equal to that of ETT3 tests depending on the elastic or plastic behavior assumption. Even though the real values in these ranges are not known, the number of cycles to failure of NP2 and NP3 tests are respectively 5×10^4 and 6×10^4 compared to 10^5 for ETT3. NP1 equivalent strain amplitude is similarly roughly equal to ETT1 and ETT2 ones, but its lifetime is once more shorter.

The potential link between the significant residual plastic strain and the early failure of the corresponding specimens is still under investigation. First post-mortem fracture observations suggest that the fatigue crack leading to failure may be not initiated by the usual fatigue mechanisms. For example, multiple fatigue cracks initiate *perpendicular to the cyclic load* for the test with low constant load (NP2), as seen in Figure 13a. On the contrary multiple ductile cracks open *perpendicular to the constant load* during the test at maximum constant load (NP3) as shown in Figure 13b. In this last test, a unique fatigue crack propagates through the gauge zone in mode I, normal to the cyclic loading, starting from one of these ductile and orthogonal multiple cracks (the history of crack initiation is easily deduced from the fact that some of the small cracks are "cut" by the main one). Note the tremendous residual strain in the case of the NP3 test (the scale is the same for both pictures).

Figure 13 : Post-mortem micrograph of specimens submitted to non-proportional loadings. The cyclic load is vertical. Central area of the gauge zone for (a) NP2 test and (b) NP3 test. (Optical microscop x100).

Concerning NP1 test, the uniaxial cyclic loading with zero mean load in the transverse direction together with a ratio of strain amplitudes equal to 0.5 between the transverse direction and the cyclic direction could tend to assimilate this test to a uniaxial fatigue test, provided a completely plastic behavior is assumed for the material. The smaller number of cycles to crack initiation obtained with NP1 compared to the uniaxial fatigue curve could partially be explained by a scale effect previously evocated between effective surface of different specimen geometries. With such a hypothesis, the comparison between results of NP1 test and ETT1 or ETT2 tests suggest that the biaxiality effect is rather weak. However, one must keep in mind that in fact, despite a zero load applied along the second axis, the stress and strain states in the centre of the gauge zone are not *stricto sensu* uniaxial because of structural effects. For a quantitative conclusion on the biaxiality effect one needs more data and a dedicated experimental campaign.

6 Conclusion

The goal of the present experimental study was to determine the biaxial fatigue behaviour of 304L austenitic stainless steel and to allow for fatigue predictions under multiaxial loading conditions. Such austenitic steels behave plastically even in High Cycle Fatigue. This feature has been recovered for biaxial loading cases. Detailed biaxial HCF results have been presented for type 304L steel thanks to modern measurements, for instance using Digital Image Correlation combined with a multiscale stroboscopic image acquisition set-up. One has focused first on the experimental protocol. The results presented then have been obtained for two different loading paths (Equibiaxial Tension-Tension and Non-Proportional with a constant lateral load).

The experiments concern a maltese cross specimen biaxially loaded by the versatile LMT-Cachan ASTREE testing machine. Except for the force signal, the test data are

measured from full-field measurements. During testing, a first camera focuses on the whole specimen when CorreliQ4 Digital Image Correlation (DIC) software is used to detect crack initiation. The variations of the strains during cyclic loading are measured thanks to an "optical strain gauge" that relies on three main points. First, a dedicated camera and a beam splitter set-up is used to acquire high resolution pictures of a small area of the same side of the specimen, in the centre of the gauge. Second it is triggered during cyclic loading according to a sub-sampling (stroboscopic) method. Last the strains are calculated thanks to the DIC software. On the other side of the specimen, two different devices are used. In some cases a similar "optical strain gauge" set-up is put in place to detect dynamic bending phenomenon. In other cases an *in-situ* microscopy set-up is used to record the crack initiation and propagation among the machine striae. The "optical strain gauge" protocol is validated by comparison with standard strain gauge measurements. The loading and clamping are also validated by strain gauge measurement. From a general point of view, the major advantage of this experimental protocol is that it allows for the knowledge of the real and local testing conditions.

Nine biaxial fatigue tests have been performed, up to 10^6 cycles. A general trend is clearly noticeable for the studied type 304L steel. The non-proportional tests with a cyclic load applied in one direction and a constant lateral load in the other direction turn out to be particularly damaging. The important residual strains due to ratchetting partially explain the early fatigue crack initiation encountered in such loadings. Several specimens have still to be tested with a loading ratio equal to -1 in order to investigate in a quantitative manner the biaxiality effect (comparison with uniaxial data) and the mean stress effect under biaxial loading (comparison with present ETT results). Polished specimens should also be tested to study a possible surface finish effect.

Appendix A: Two scale damage model

The two scale damage model is an incremental damage model (Desmorat *et al.*, 2007; Lemaitre and Doghri, 1994) which consists in:

- a mesoscopic elastic behaviour $\boldsymbol{\sigma}(t)$, $\boldsymbol{\varepsilon}(t)$ at the Representative Volume Element (RVE) scale (below the yield stress σ_y), *i.e.* at structure Gauss points,
- a scale transition law mesoscale (RVE) $\rightarrow$ microscale (the defects scale), of Eshelby-Kröner type,
- plasticity (von Mises type) with linear kinematic hardening $\mathbf{X}^{\mu}$ coupled with damage $D^{\mu} = D$ (Lemaitre type) constitutive equations at microscale ($\boldsymbol{\varepsilon}^{\mu}, \boldsymbol{\varepsilon}^{\mu e}, \boldsymbol{\varepsilon}^{\mu p}$ are the total, elastic and plastic strains at microscale).

The associated set of constitutive equations is

$$\begin{cases} \varepsilon = \dfrac{1+\nu}{E}\sigma - \dfrac{\nu}{E} tr\sigma I \\ \varepsilon^{\mu} = \dfrac{1}{1-\beta D}\left[\varepsilon + \dfrac{(\alpha-\beta)D}{3(1-\alpha D)} tr\varepsilon I + \beta\left((1-D)\varepsilon^{\mu p}\right)\right] \\ \varepsilon^{\mu} = \varepsilon^{\mu e} + \varepsilon^{\mu p} \\ \varepsilon^{\mu e} = \dfrac{1+\nu}{E}\tilde{\sigma}^{\mu} - \dfrac{\nu}{E} tr\tilde{\sigma}^{\mu} I \quad \text{with} \quad \tilde{\sigma}^{\mu} = \dfrac{\sigma^{\mu}}{1-D} \\ \mathrm{f}^{\mu} = \left(\tilde{\sigma}^{\mu} - \mathbf{X}^{\mu}\right)_{eq} - \sigma_f^{\infty} \\ \dot{\varepsilon}^{\mu p} = \dfrac{3}{2}\dfrac{\tilde{\sigma}^{\mu D} - \mathbf{X}^{\mu}}{\left(\tilde{\sigma}^{\mu D} - \mathbf{X}^{\mu}\right)_{eq}}\dot{p}^{\mu} \\ \dot{\mathbf{X}}^{\mu} = \dfrac{2}{3} C_y (1-D)\dot{\varepsilon}^{\mu p} \\ \dot{D} = \left(\dfrac{Y^{\mu}}{S}\right)^{s}\dot{p}^{\mu} \\ D = D_c \rightarrow \text{crack initiation} \\ \mathrm{f}^{\mu} \le 0, \quad \dot{p}^{\mu} \ge 0, \quad \mathrm{f}^{\mu}\dot{p}^{\mu} = 0 \end{cases} \tag{A.1}$$

where superscripts μ stand for "value at microscale", with E, ν, α and β the elasticity and Eshelby parameters

$$\alpha = \frac{1+\nu}{3(1-\nu)} \tag{A.2}$$

$$\beta = \frac{2}{15}\frac{4-5\nu}{1-\nu} \tag{A.3}$$

The yield criterion only considers linear kinematic hardening $\mathbf{X}^{\mu}$ (of plastic modulus C_y) and uses the fatigue limit σ_f^{∞} as yield stress at microscale

$$\mathrm{f}^{\mu} = (\boldsymbol{\sigma}^{\mu} - \mathbf{X}^{\mu})_{eq} - \sigma_f^{\infty} \tag{A.4}$$

Damage is governed by the accumulated plastic strain at microscale p^{μ}. The driving force for damage introduces a micro-defects closure parameter h=0.2 acting on negative stresses only,

$$Y^{\mu} = \frac{1+\nu}{2E}\left[\frac{\left\langle\boldsymbol{\sigma}^{\mu}\right\rangle^{+} : \left\langle\boldsymbol{\sigma}^{\mu}\right\rangle^{+}}{(1-D)^2} + h\frac{\left\langle\boldsymbol{\sigma}^{\mu}\right\rangle^{-} : \left\langle\boldsymbol{\sigma}^{\mu}\right\rangle^{-}}{(1-hD)^2}\right] - \frac{\nu}{2E}\left[\frac{\left\langle tr\boldsymbol{\sigma}^{\mu}\right\rangle_{+}^{2}}{(1-D)^2} + h\frac{\left\langle tr\boldsymbol{\sigma}^{\mu}\right\rangle_{-}^{2}}{(1-hD)^2}\right] \tag{A.5}$$

The damage parameters are the damage strength S, the damage exponent s and the critical damage at crack initiation D_c.

Appendix B: Detailed measurement set-up

The Digital Single Lens Reflex (DSLR) camera is an EOS 350D (Canon, 3456 x 2304 pixels) with a macro prime lens (SIGMA 105 mm F 2,8 DG Macro EX). The shutter release lag of a DSLR camera is scattered over several ms (*e.g.* the difference between minimum and maximum values of the shutter lag for the EOS 400D is about 15 ms (DOC-DIY, 2010)), so

that acquisitions with this camera during a loading at 10 Hz are not possible with continuous lighting.

The CCD camera is a Pixelfly (1360 x 1024 pixels, 12 bits, 12 fps) with a telecentric lens (1X in-line illumination telecentric lens, Edmund Optics).

The optical set-up is composed of a beam-splitter (TECHSPEC® standard cube beamsplitter 50 mm, Edmund Optics) and a prism (TECHSPEC® high-tolerance right angle prisms, 50 mm, Edmund Optics). The lighting set-up is composed of two continuous tungsten lightning spots (DEDOLIGHT 400W) and two LED spots (Luxeon 3x3W).

Concerning the sub-sampling method, the transfer time needed by the camera between two images in external trigger mode is about 1 s, so that integer N is set to 10. The value of n has to be a compromise between a fine enough sub-sampling and the risk of artefacts due to a change of the cyclic behaviour of the material during the recording of the n images. Integer n is set to 20, so that the total recording time is equivalent to 200 cycles. Last, the integration time is set to 2.5 ms, much less than the load period of 100 ms, to prevent the blurring by motion.

The other set of digital camera and telecentric lens used on the upper side of the specimen is composed of a DALSA camera (Pantera 1M30, 1024 x 1024 pixels, 12 bits, 30 fps) and a Edmunds Optics lens (1.0X Gold Series Telecentric Lens (2/3" Series)).

The microscopy set-up is composed of an EOS 40D camera (Canon, 3 888 x 2 592 pixels) mounted on a Long Distance Microscope (LDM, Questar QM100, about x100 in the present conditions).

References

Akamatsu, M., Chevallier, E., 2001. Caractérisation chimique et mécanique des matériaux approvisionnés pour l'étude du comportement en fatigue des aciers inoxydables austénitiques, Technical note HT-42/00/020/A, EDF, R&D.

Andrew, J.M.H., Ellison, E.G., 1973. A testing rig for cycling at high biaxial strains, The Journal of Strain Analysis for Engineering Design Professional Engineering Publishing ISSN0309-3247. 8(3), 2041-3130.

Barbier, G., 2009. Fatigue biaxiale à grand nombre de cycles : étude expérimentale, endommagement à deux échelles probabiliste, PhD thesis, ENS Cachan.

Bari S., Hassan, T., 2000. Anatomy of Coupled Constitutive Models for Ratchetting Simulation, Int. Jal of Plasticity. 16, 381-409.

Bedkowski, W., 1994. Determination of Critical Plane and Effort Criterion in Fatigue Life Evaluation for Materials under Multiaxial Random Loading. Experimental Verification Based on Fatigue Tests of Cruciform Specimens. Proc. 4th ICB/MF, May 31 - June 3, 1994, Paris, 435 – 447.

Besnard, G., Hild, F., Roux., S., 2006. "Finite-element" displacement fields analysis from digital images: application to Portevin-Le-Châtelier bands, Exp. Mech. 46(6), 789–804.

Bocher, L., Delobelle, P. Robinet, P., Feaugas, X., 2001. Mechanical and Microstructural Investigations of an Austenitic Stainless Steel under Non-Proportional Loadings in Tension-Torsion- Internal and External Pressure, Int. Jal of Plasticity. 17, 1491-1530.

Bonnand, V., Chaboche, J.L., Cherouali, H., Gomez, P., Kanouté, P., Pacou, D., Paulmier, P., Ostoja-Kuczynski, E., Vogel, F., 2009. Experimental and theoretical comparison of some multiaxial fatigue design criteria in the context of life assessment of rotating parts in turboengines. in, ICAF 2009, Proceedings of the 25th Symposium of the International Committee on Aeronautica l Fatigue, Rotterdam, The Netherlands,27–29 May 2009.

Bouvet, C., Calloch, S., Lexcellent, C., 2002. Mechanical Behavior of a Cu-Al-Be Shape Memory Alloy Under Multiaxial Proportional and Nonproportional Loadings, J. Eng. Mater. Technol. 124, 112.

Calloch, S., Marquis, D., 1999. Triaxial tension–compression tests for multiaxial cyclic plasticity, Int. Jal of Plasticity, 15(5), 521-549.

Chaboche, J.L., Lesne, P.M., 1988. A non-linear continuous fatigue damage model, Fatigue Fract Engng Mater Struct. 11, 1–17.

Chaboche, J.-L., 1991. On Some Modifications of Kinematic Hardening to Improve the Description of Ratchetting Effects, Int. Jal of Plasticity. 7, 661-678.

Chapuliot, S., Gourdin, C., Payen, T., Magnaud, J.P., Monavon, A., 2005. Hydro-thermal-mechanical analysis of thermal fatigue in a mixing tee, Nuclear Engineering and Design. 235, 575–596.

Charkaluk, E., Constantinescu, A., 2000. An energetic approach in thermomechanical fatigue for silicon molybdenum cast iron. Materials at High Temperatures. 17(3), 373–380.

Chellapandi, P., Chetal, S.C., Baldev, R., 2009. Thermal striping limits for components of sodium cooled fast spectrum reactors. Nucl. Eng. Des. 239(12), 2754-2765.

Cipiere, M.-F., Goltrant, O., 2002. Circuit RRA N4 – Incident de Civaux 1 – Endommagement par fatigue thermique de tuyauteries situées dans les zones de mélange, Fontevraud V, Contribution of material investigations to the resolution of problems encountered in PWR's, France, 23-27 septembre 2002.

Colin, J., Fatemi, A., Taheri, S., 2010. Fatigue behavior of Stainless Steel 304L Including Strain Hardening, Prestraining, and Mean Stress Effects, ASME J. Eng. Mat. Tech. 132 online.

Cognard, J., Feuardent, V., Virely, J.-M., 1997. Integrated design and manufacturing in mechanical engineering. section optimisation of a structure for biaxial mechanical tests. In Publisher Kluwer Acad. Publ.. Editor Chedmail,P.

Crossland, B., 1956. Effect of large hydrostatic pressures on the torsional fatigue strength of an alloy steel. In: Proc. of the Inter. Conf. on Fatigue Metals. Inst. Mech. Engrg. 138–149.

Dang Van, K., 1973. Sur la résistance à la fatigue des métaux. Technical Report 3ème fascicule, Sciences et techniques de l'armement, Mémorial de l'artillerie française.

Dang Van, K., Papadopoulos, I., 1999. High Cycle Metal Fatigue. Springer, New York.

Delobelle, P., Robinet, P., Bocher, L., 1995. Experimental Study and Phenomenological Modelization of Ratchet under Uniaxial and Biaxial Loading on an Austenitic Stainless Steel, Int. Jal of Plasticity. 11, 295-330.

Desmorat, R., Pauget, F., Sermage, J.-P., 2006. DAMAGE-2005 : a post-processor for High Cycle Fatigue under complex thermomechanical loading, PVP 2006/ICPVT 11 -ASME Pressure Vessels and Piping Division Conference, Vancouver, BC, Canada, 23-27 july 2006.

Desmorat, R., Kane, A., Seyedi, M., Sermage, J.-P., 2007. Two scale damage model and related numerical issues for thermo-mechanical High Cycle Fatigue, European Journal of Mechanics - A/Solids. 26, 909-935.

Doudard, C., Poncelet, M., Calloch, S., Boue, C., Hild, F., Galtier, A., 2007. Determination of an HCF criterion by thermal measurements under biaxial cyclic loading, Int. Jal of Fatigue. 29(4), 748–757.

Eichelmann, G. H., Hull, F.C., 1953. The effect of composition on the temperature of spontaneous transformation of austenite to martensite in 18.8 stainless steel, Transactions of the ASM. 45, 77.

Faidy, C., Le Courtois, T., de Fraguier, E., Le Duff, J. A., Le François, A., Dechelotte, J., 2000, Thermal fatigue in French RHR system. In: International conference on fatigue of reactor components, Napa, California, USA, 31 July – 2 August 2000.

Fatemi, A., Yang, L., 1998. Cumulative fatigue damage and life prediction theories: a survey of the state of the art for homogeneous materials, Int. Jal of Fatigue. 20(1), 9-34.

Fissolo, A., Amiable, S., Ancelet, O., Mermaz, F., Stelmaszyk, J.M., Constantinescu, A., Robertson, C., Vincent, L., Maillot, V., Bouchet, F., 2009. Crack initiation under thermal fatigue: An overview of CEA experience. Part I: Thermal fatigue appears to be more damaging than uniaxial isothermal fatigue, Int. Jal of Fatigue. 31(3), 587-600.

Gerland, M., Alain, R., Ait Saadi, B., Mendez, J., 1997. Low cycle fatigue behaviour in vacuum of a 316L-type austenitic stainless steel between 20 and 600°C – Part II: Dislocation structure evolution and correlation with cyclic behaviour, Mat. Sc. and Eng. A. 229, 68-86.

Hamam, R., Hild, F., Roux, S., 2007. Stress intensity factor gauging by digital image correlation : Application in cyclic fatigue, Strain. 43, 181-192.

Hild, F., Roux, S., 2005. Digital Image Correlation: from measurement to identification, submitted.

Itoh, T., Sakane, M., Ohnami, M., 1994. High temperature multiaxial low cycle fatigue of cruciform specimen. Journal of Engineering Materials and Technology. 116(91), 90–98.

Kaleta, J., Zietek, G., 1998. Representations of cyclic properties of austenitic steels with plasticity-induced martensitic transformation, Fat. Fract. Eng. Mat. Struct. 21, 955-964.

Kimura, N., Miyakoshi, H., Kamide, H., 2007. Experimental investigation on transfer characteristics of temperature fluctuation from liquid sodium to wall in parallel triple-jet, International Journal of Heat and Mass Transfer. 50, 2024–2036.

Kurpp, U., Christ, H. J., Lezuo, P., Maier, H.J., Teteruk, R.G., 2001. Influence of carbon concentration on martensitic transformation in metastable austenitic steels under cyclic loading conditions, Mat. Sci. Eng. A. 319(21), 527-530.

Lanza, G., 1886. Strength of shafting subject to both twisting and bending. trans. ASME. 8, 130.

Lefebvre, D., Chebl, C., Thibodeau, L., Khazzari, E., 1983. A high-strain biaxial-testing rig for thin-walled tubes under axial load and pressure, Exp. Mech. 23(4), 384-392.

Lemaitre, J., 1992. A Course on Damage Mechanics. Springer-Verlag, Berlin.

Lemaitre, J., Doghri, I., 1994. Damage 90: a post-processor for crack initiation. Comp. Methods Appl. Mech. Engrg. 115, 197–232.

Lemaitre, J., Sermage, J.-P., Desmorat, R., 1999. A two scale damage concept applied to fatigue, Int. Jal of Fracture. 97, 67-81.

Lemaitre, J., Chaboche, J.L., Benallal, A., Desmorat, R., 2009. Mécanique des matériaux solides, 3rd Edition, Dunod, Paris.

Le Roux, J.-C., 2004. Influence de paramètres métallurgiques et d'essai sur l'amorçage des fissures de fatigue en déformation imposée des aciers inoxydables austénitiques, Projet t2-00-04 (domzone), Note EDF R&D HT-26/03/056/B.

Manson, S.S., Hirschberg, M., 1964. Fatigue: An Interdisciplinary Approach, Syracuse University Press, Syracuse, NY.

Marin, J., 1949. Résistance des métaux à la fatigue par contraintes biaxiales. Jal of Applied Mechanics. 16, 383.

Mason, W., 1917. Alternating stress experiments. Proc. Inst. Mech. Eng. 1, 187–190.

McClaren, S.W., Terry, F.L., 1963. Characteristics of aerospace materials subjected to biaxial static and fatigue loading conditions. A.S.M.E. Paper 63-WA-315.

McNeill, S., Peters, W., Sutton, M., 1987. Estimation of stress intensity factor by digital image correlation, Eng. Fract. Mech. 28(1), 101-112.

Molinie, E., 2002. Caractéristiques des tronçons RRA 900-1300 déposés : synthèse et enseignements acquis, Fontevraud V, Contribution of materials investigations to the resolution of problems encountered in PWR's, France, 23-27 septembre 2002.

Müller-Bollenhagen, C., Zimmermann, M., Christ, H.-J., 2010. Very High Cycle Fatigue behaviour of austenitic stainless steel and the effect of strain-induced martensite Int. Jal of Fatigue. 32(6), 936-942.

Ohno, N., Wang, J.D., 1993. Kinematic Hardening Rules with Critical State of Dynamic Recovery, Part I and II, Int. Jal of Plasticity. 9, 375-403.

Otin, S., Desmorat, R., Bambrine, B., 2007. Incremental damage laws for design of turbomachines, ICNM 5 – 5th International Conference on Nonlinear Mechanics, Shangai, China, 11 - 14 June 2007, 221-227.

Paffumi, E., Nilsson, K.-F., Taylor, N.G., 2008. Simulation of thermal fatigue damage in a 316L model pipe component, International Journal of Pressure Vessels and Piping. 85, 798–813.

Pascoe, K., De Villiers, J., 1967. Low cycle fatigue of steels under biaxial straining. Journal of Strain Analysis. 2(2), 117–126.

Portier, L., Calloch, S., Marquis, D., Geyer, P., 2000. Ratchetting under Tension-Torsion loadings: Experiments and Modelling, Int. Jal of Plasticity. 16, 303–335.

Renault, A., 2006. Technical note, FdE, LA2M2006-007 AT MET DT 345.

Rupil, J., Malésys, N., Vincent, L., Hild, F., 2009. Contribution of mechanical fatigue experiments to the improvement of a probabilistic model for the formation of crack networks under thermal fatigue, Proceeding of ESMC 2009, electronic version.

Sermage, J.-P., 1998. Fatigue thermique multiaxiale à température variable. PhD thesis, Université Pierre et Marie Curie Paris 6.

Sermage, J.-P., Lemaitre, J., Desmorat, R., 2000. Multiaxial creep fatigue under anisothermal conditions, Fatigue and Fracture of Engineering Materials & Structures. 23(3), 241–252.

Shiratori, E., Ikegami, K., 1967. A new biaxial tensile testing machine with flat specimen. Bull Tokyo Inst Technol. 82, 105–118

Sines, G., 1959. Behavior of metals under complex static and alternating stresses. In: Sines, G., Waisman, J.L. (Eds.). McGraw-Hill, New York, 145–169.

Solomon, H. D., Amzallag, C., Delair, R.E., Vallee, A.J., 2004. strain controlled fatigue of type 304L SS in Air and PWR, 3rd international conference on fatigue of reactors components, Seville 3-6 october 2004.

Stephan, J.-M., Curtit, F., Vindeirinho, C., Taheri, S., Akamatsu, M., Peniguel, C., 2002. Evaluation of the risk of damages in mixing zones: EDF R&D program, ASME PVP Conference, Canada, Vancouvert, 4-8 august 2002.

Stolarz, J., Baffie, N., Magnin, T., 2001. Fatigue short crack behavior in metastable austenitic stainless steels with different grain sizes, Mat. Sci. Eng. A. 319(21), 521-526.

Vanlanduit, S., Vanherzeele, J., Longo, R., Guillaume, P., 2009. A digital image correlation method for fatigue test experiments, J.Opt. Las. Eng. 47, 371– 378

Vincent, L., Perez, G., 2005. Etude de la fatigue d'un acier inoxydable austénitique aux faibles niveaux de chargement. Rapport d'avancement n°3. CEA Tech. Report, DMN/SRMA/LC2M/NT/2005-2742/A.

Weibull, W., 1951. A statistical distribution function of wide applicability. ASME J. Appl. Mech. 18(3), 293–297.

Wilson, I., White, D., 1971. Cruciform specimens for biaxial fatigue tests : an investigation using finite-element analysis and photoelasticcoating techniques. J. of Strain Analysis. 6(1), 27–37.

NI, 1999. National Instrument, LabVIEWTM version 5.1, user's manual (http://www.ni.com).
DOC-DIY, 2010. http://www.doc-diy.net/photo/shutter_lag/ (13/04/2010).

Table 1 : Chemical composition of studied type 304L Stainless Steel (%Wt), from (Akamatsu and Chevallier, 2001).

C	Mn	Si	P	S	Cr	Ni	Mo	Cu	N_2	Fe
0,029	1,86	0,37	0,029	0,004	18,00	10,00	0,04	0,02	0,056	Bal

Table 1: Monotonic mechanical properties for the studied type 304L stainless steel, from (Akamatsu and Chevallier, 2001).

direction	Yield stress (MPa)	Ultimate tensile strength (MPa)	Rupture elongation (%)	Reduction in area (%)
Rolling	190	577	80	81
transverse	192	578	78	77

Table 1: Definition of the loading paths.

		F_1^{max} (kN)	F_2^{max} (kN)	R_{F1}	R_{F2}
Equibiaxial Tension-Tension (ETT)	ETT1	28	28	0.1	0.1
	ETT2	31	31	0.1	0.1
	ETT3	38	38	0.1	0.1
Non-Proportional tension-tension with constant load (NP)	NP1	38	0	0.1	1
	NP3	38	19	0.1	1
	NP3	38	38	0.1	1

Table 1: Non-Proportional Tension-Tension with constant load tests results.
The strain field shows the increment of residual strain during the last series of cycles, in the meniscus of the gauge zone. Depending on the crack orientation, ε_{xx} or ε_{yy} is plotted to better visualization. The circle stands for the gauge zone limit. The strain scale is the same for every test and the gauge diameter (black circle) is 30mm.

TEST	Axis	F^{max} (kN)	R_F	$\Delta\varepsilon/2$ (%)	$\varepsilon_{res}(N_\iota)$ (%)	N_i	Strain field at N_i
NP1	x	38.0	0.1	0.145	9.706	[275 000 ; 280 000]	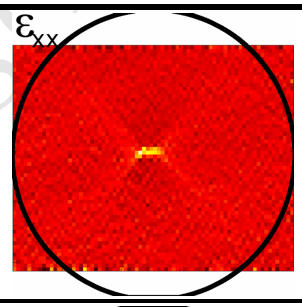
	y	0.0	1.0	0.072	-5.693		
NP2	x	38.0	0.1	0.178	3.630	[30 000 ; 40 000]	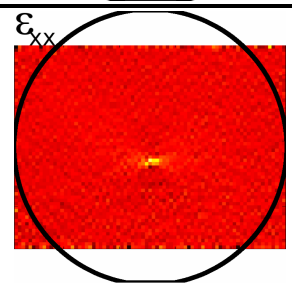
	y	19.3	0.97	0.085	-0.222		
NP3	x	38.6	0.14	0.205	-0.220	[45 000 ; 55 000]	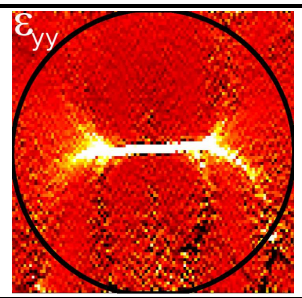
	y	39.5	0.97	0.125	17.430		

Table 1: Equibiaxial Tension-Tension (ETT) tests results.

TEST	Axis	F^{max} (kN)	R_F	$\Delta\varepsilon/2$ (%)	$\varepsilon_{res}(N_t)$ (%)	N_i	Strain field at N_i 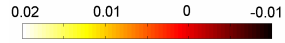
ETT1	x	27.4	0.15	0.070*	0.760	no initiation after $1.5\ 10^6$ cycles	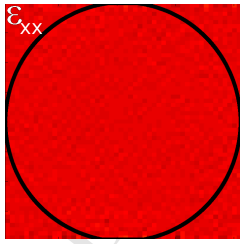
	y	28.6	0.13	0.093*	1.330		
	* $\Delta\varepsilon/2$ unavailable at half-life (technical problem). Values are given after 1000 cycles.						
ETT2(1)	x	30.0	0.08	0.077*	1.330	[480000 ; 490000]	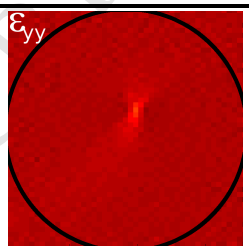
	y	30.2	0.06	0.075*	2.061		
	* $\Delta\varepsilon/2$ unavailable (technical problem). Given values come from ETT2(2).						
ETT2(2)	x	31.0	0.07	0.077	1.700	no initiation after 10^6 cycles	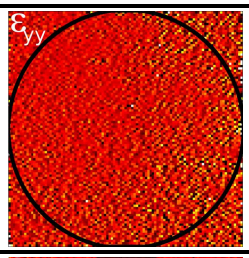
	y	31.0	0.08	0.075	1.566		
ETT3(0) *	x	38.0	0.10	0.100	6.145	[105000 ; 115000]	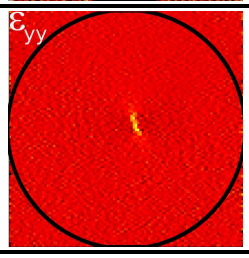
	y	38.0	0.10	0.099	5.021		
	* performed on ETT2(2) specimen						
ETT3(1)	x	37.5	0.11	0.100*	3.582	[120000 ; 125000]	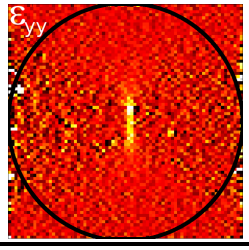
	y	38.1	0.11	0.099*	5.329		
	* $\Delta\varepsilon/2$ unavailable (technical problem). Given values come from ETT3(0).						
ETT3(2)	x	37.7	0.11	0.091	5.613	[80000 ; 83000]	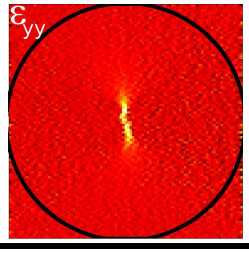
	y	36.9	0.11	0.086	8.750		

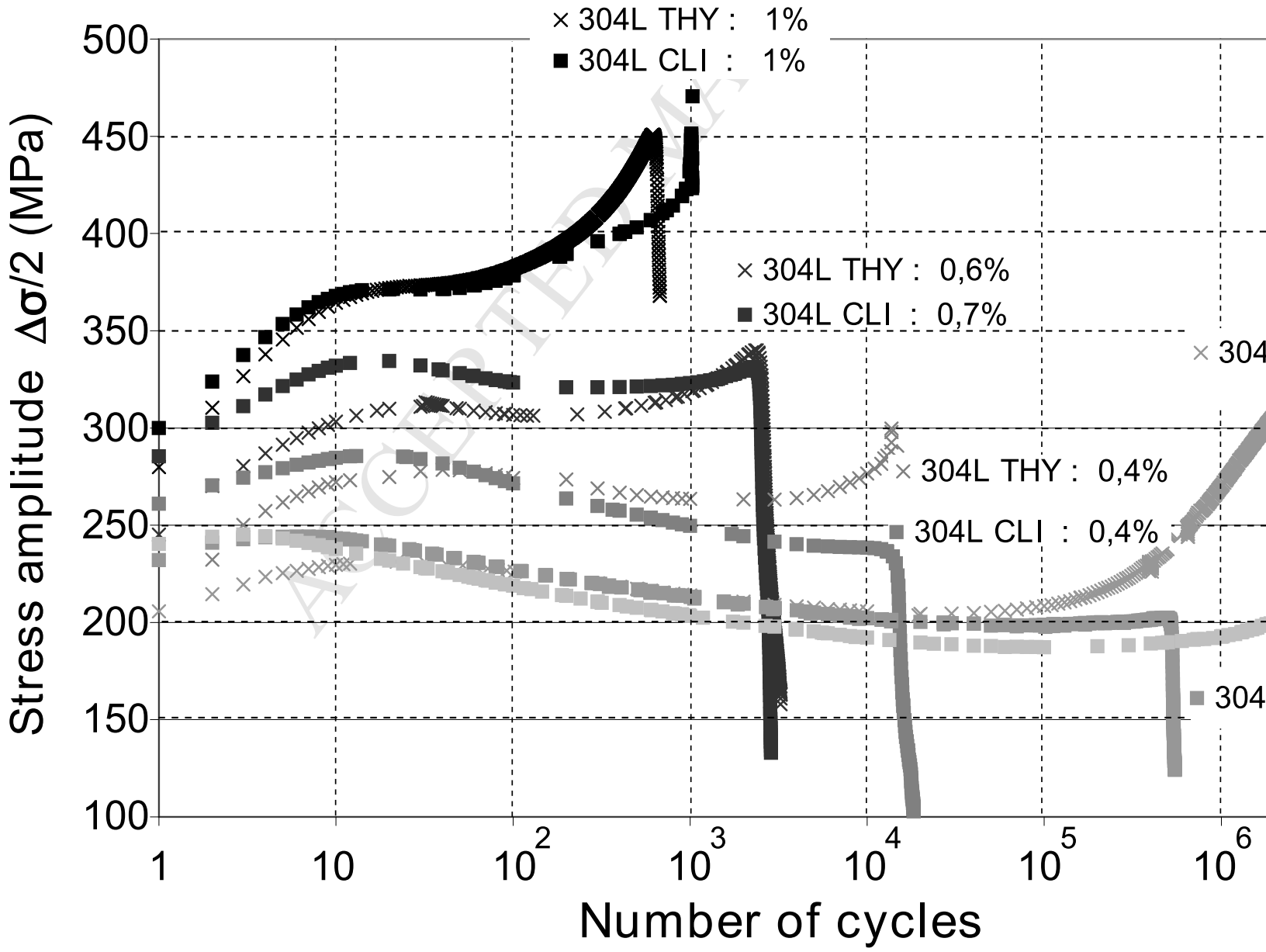

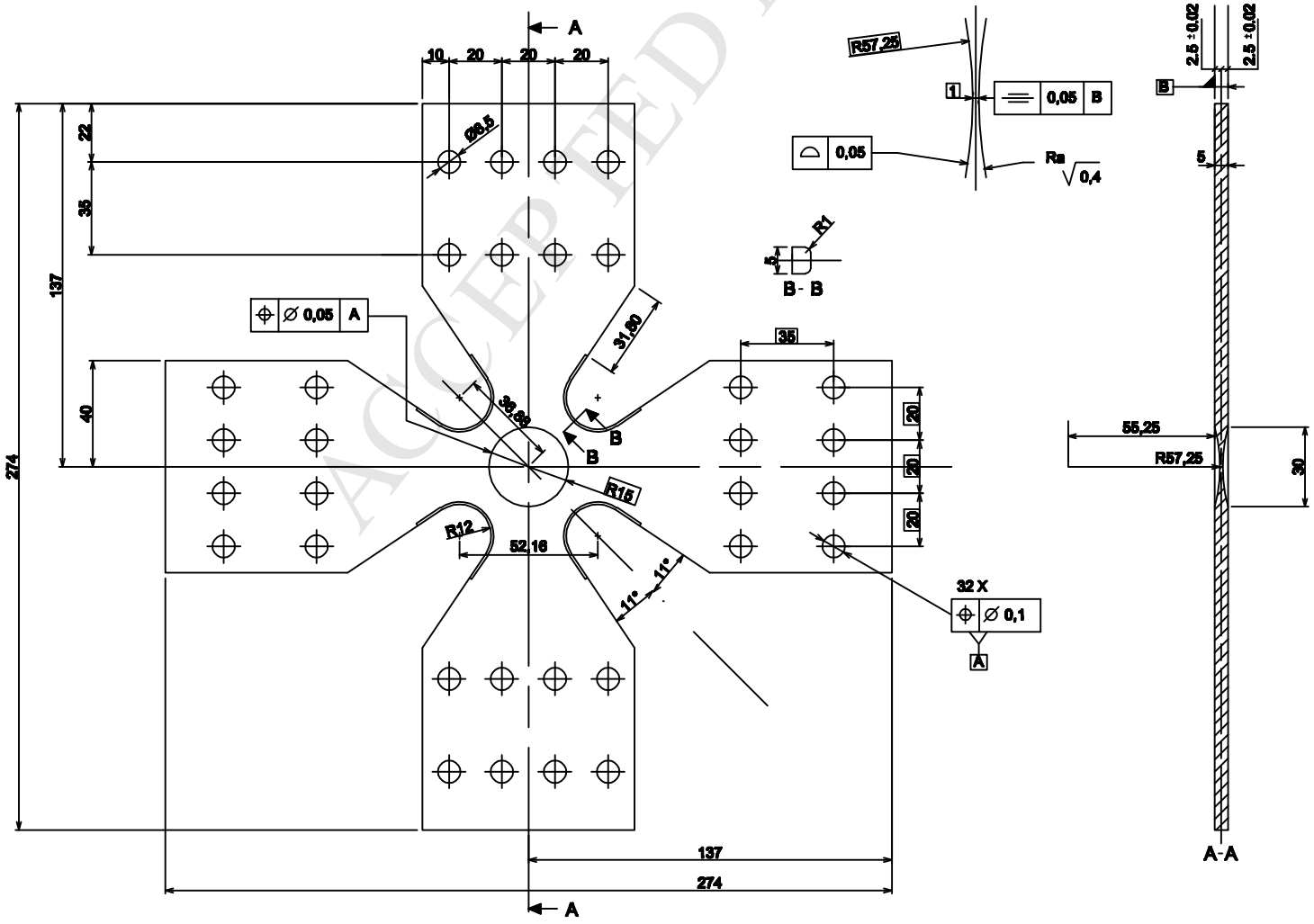

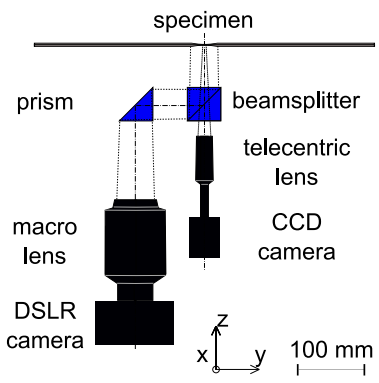

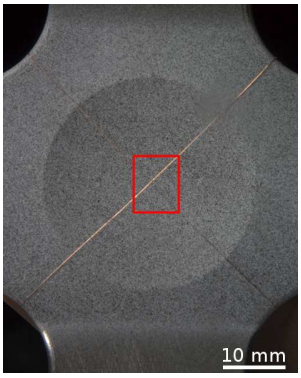

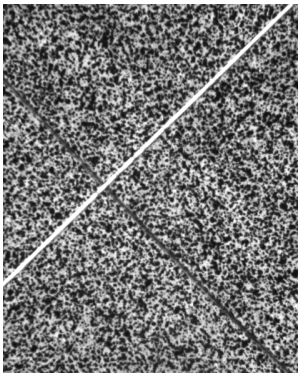

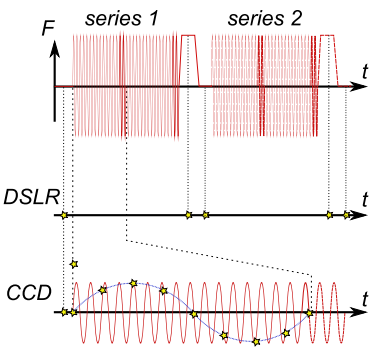

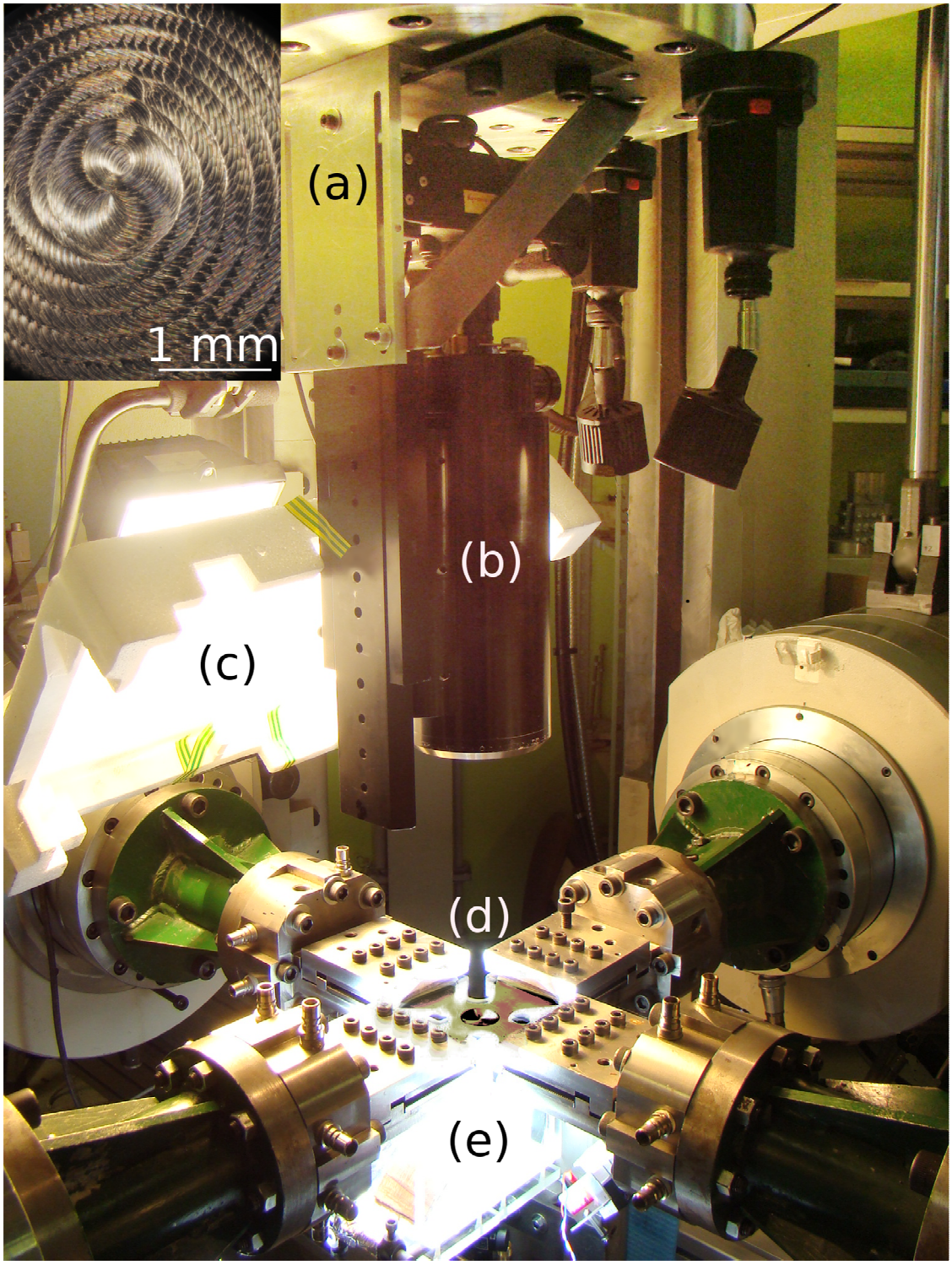
1 mm
(a)
(b)
(c)
(d)
(e)

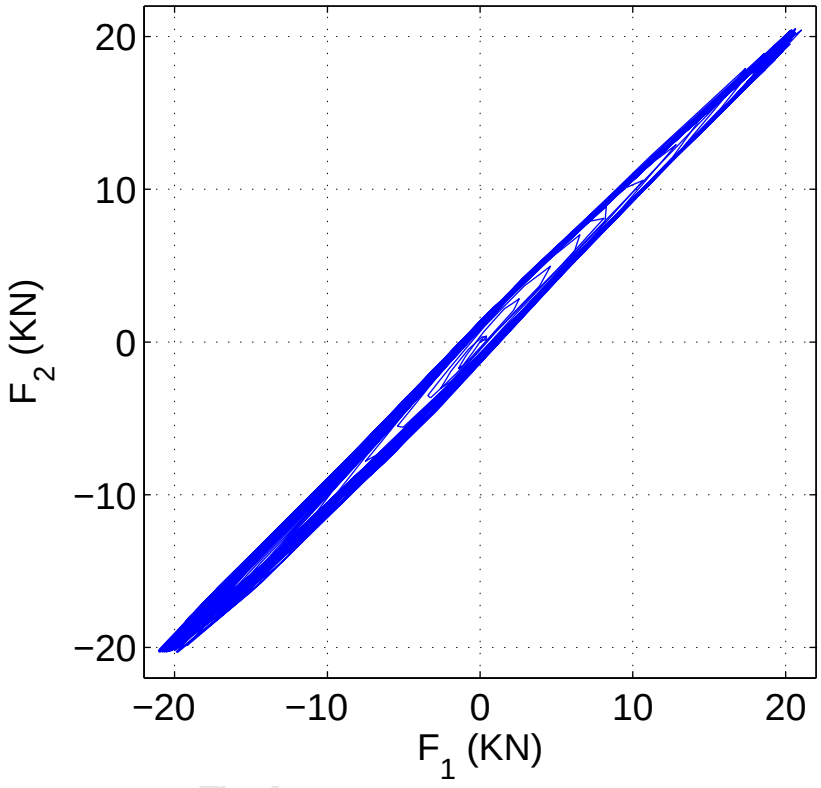

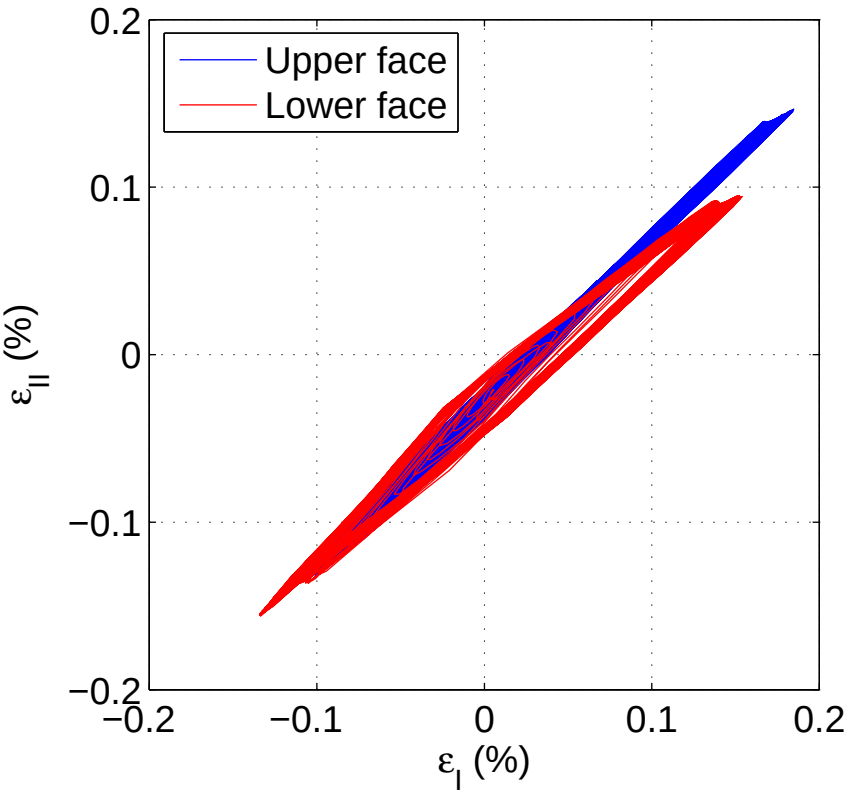

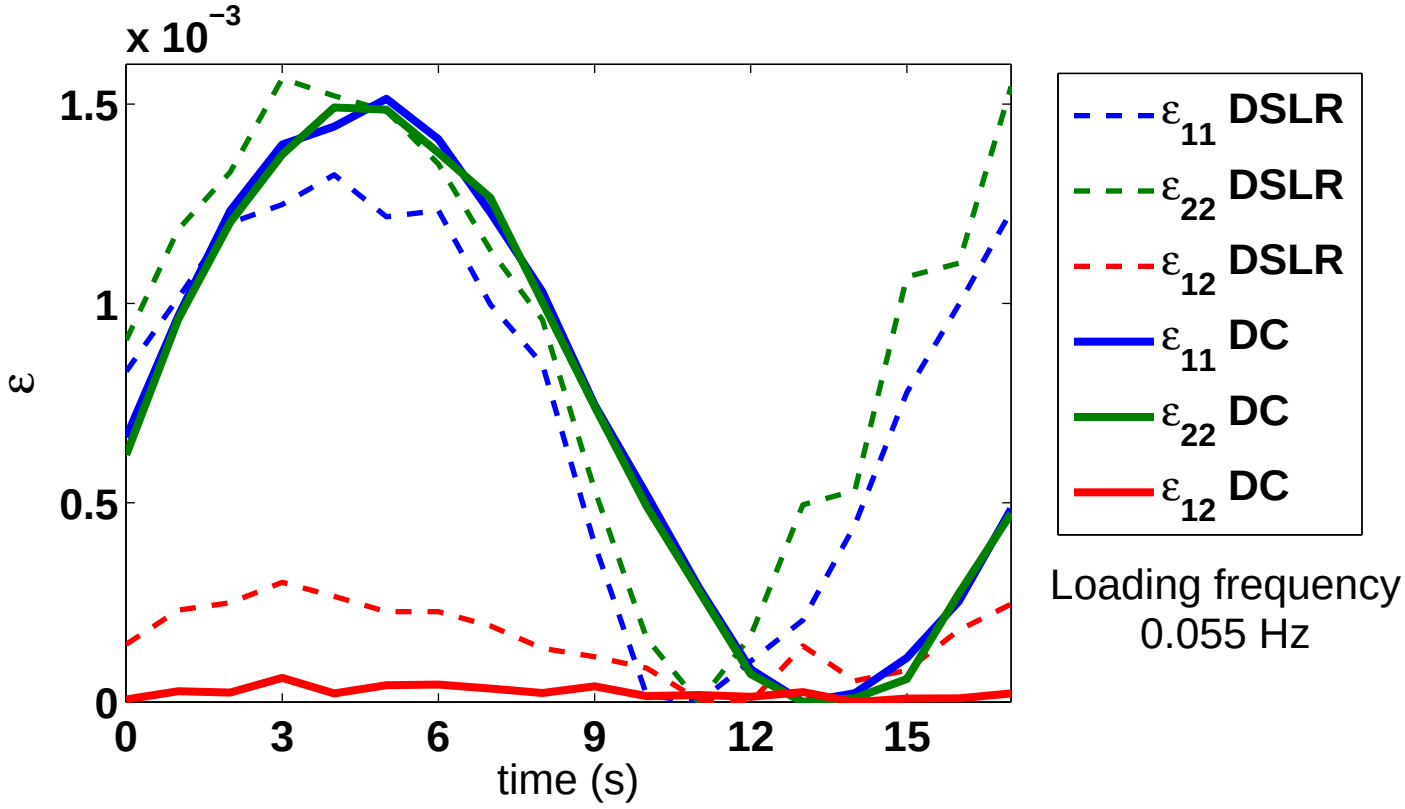

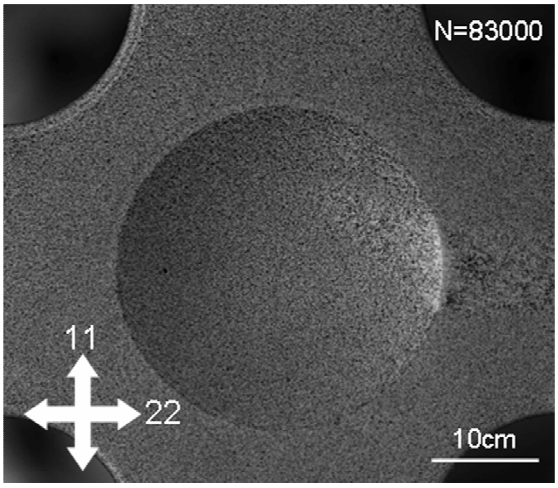

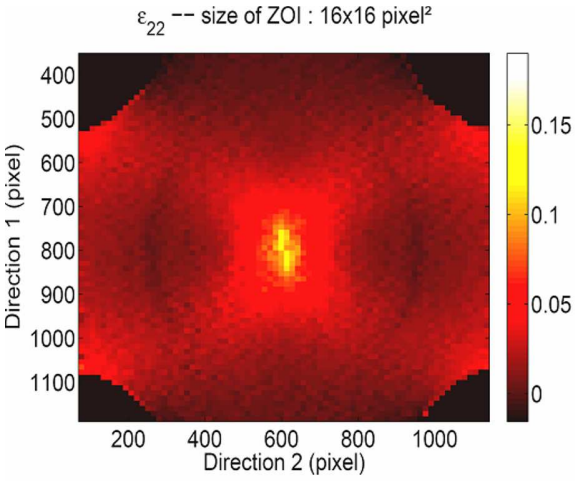

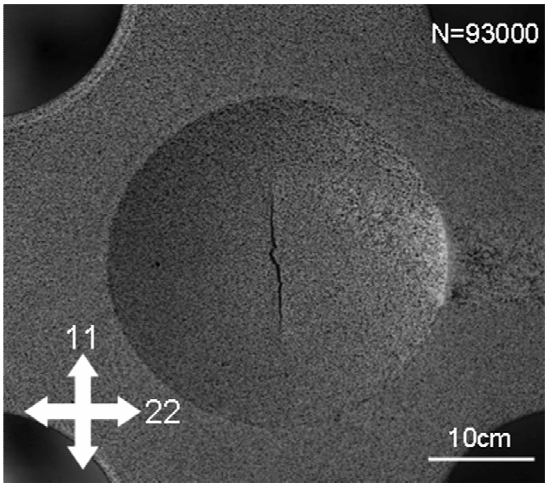

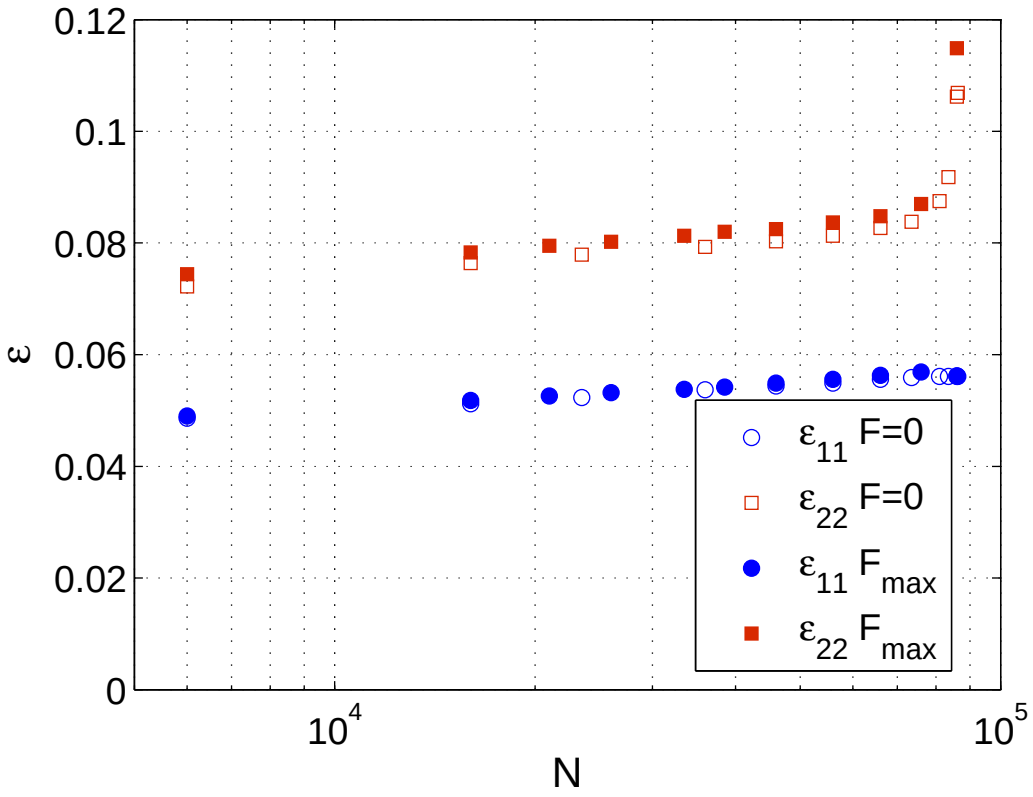

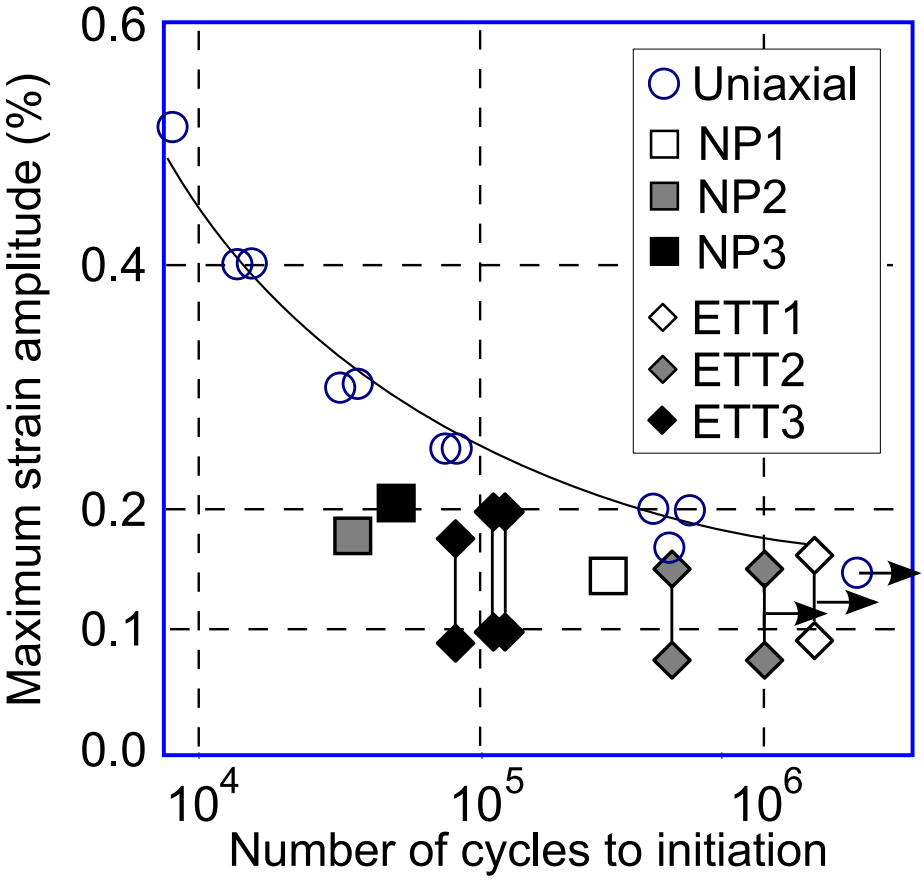
0.6
0.4
0.2
0.1
0.0
Maximum strain amplitude (%)
10^4
10^5
10^6
Number of cycles to initiation
Uniaxial
NP1
NP2
NP3
ETT1
ETT2
ETT3

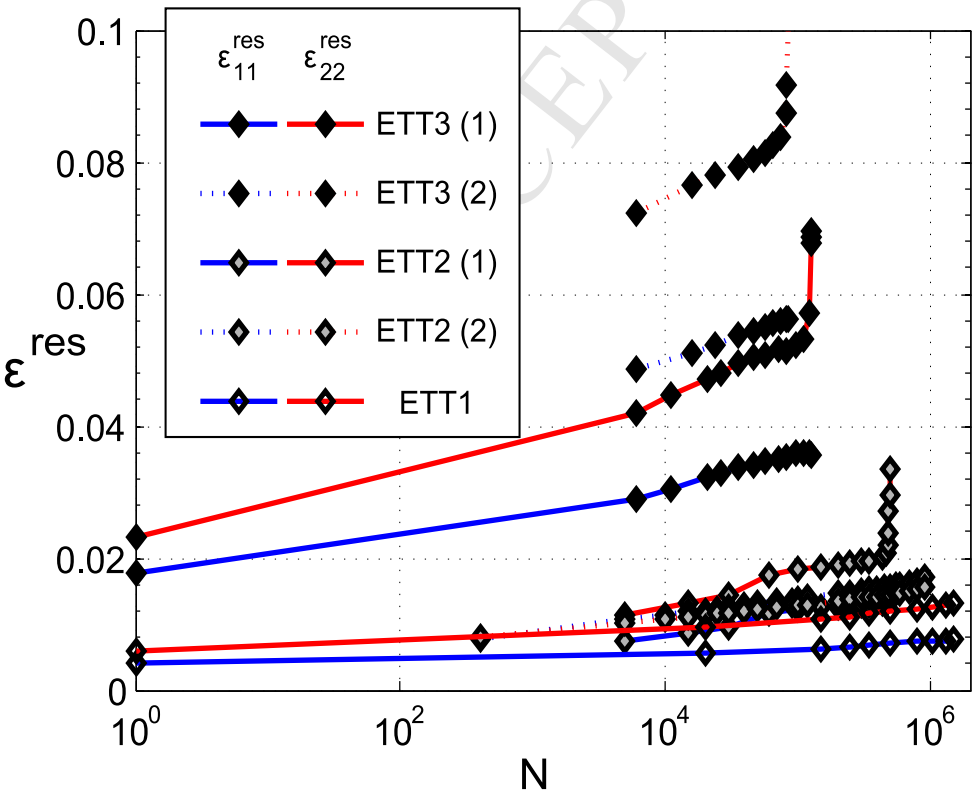

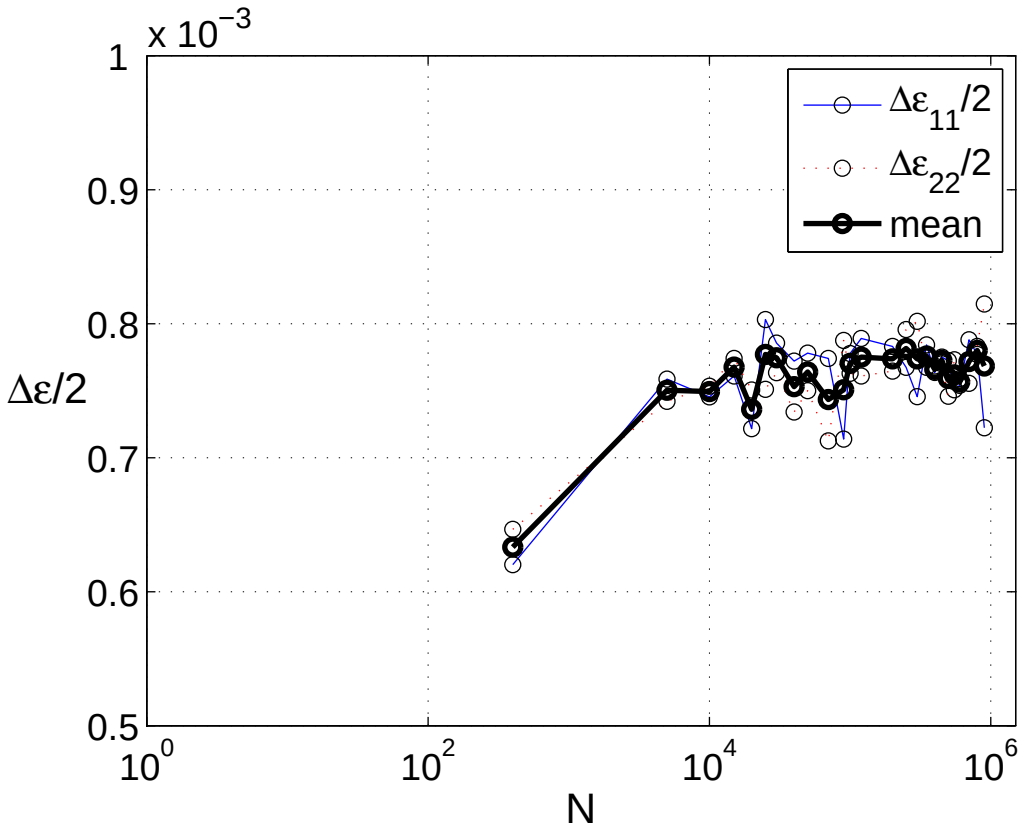

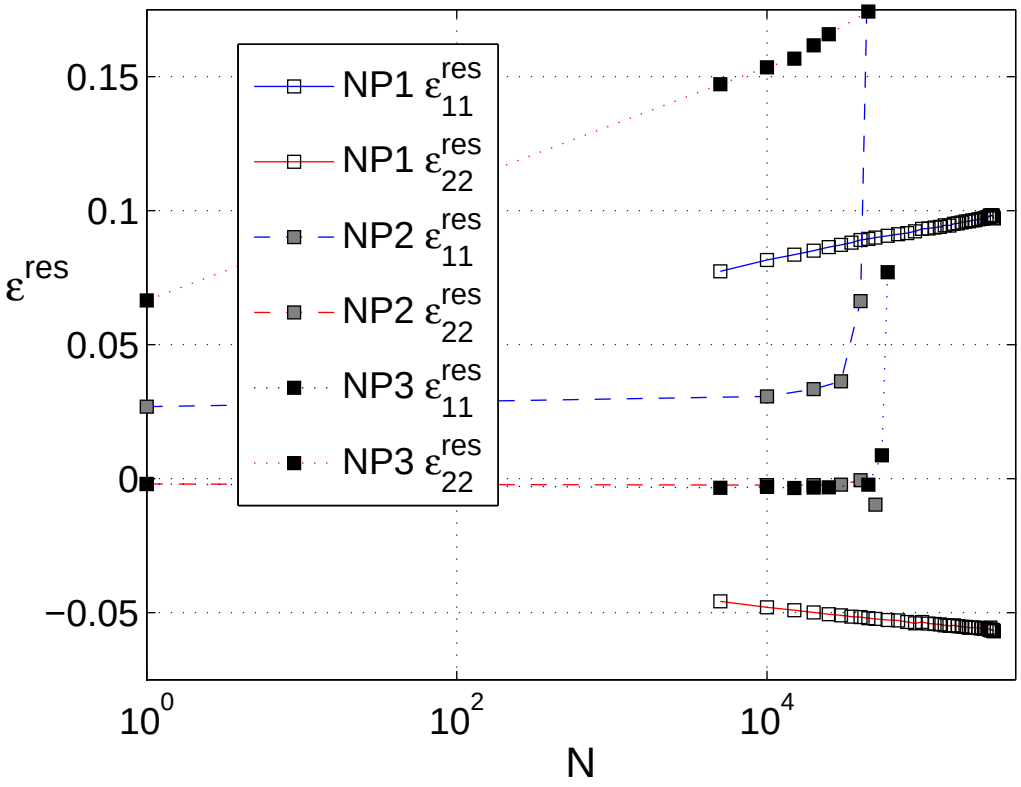
0.15
0.1
0.05
0
−0.05
ε^{res}
10^0
10^2
10^4
N
NP1 ε^{res}_{11}
NP1 ε^{res}_{22}
NP2 ε^{res}_{11}
NP2 ε^{res}_{22}
NP3 ε^{res}_{11}
NP3 ε^{res}_{22}

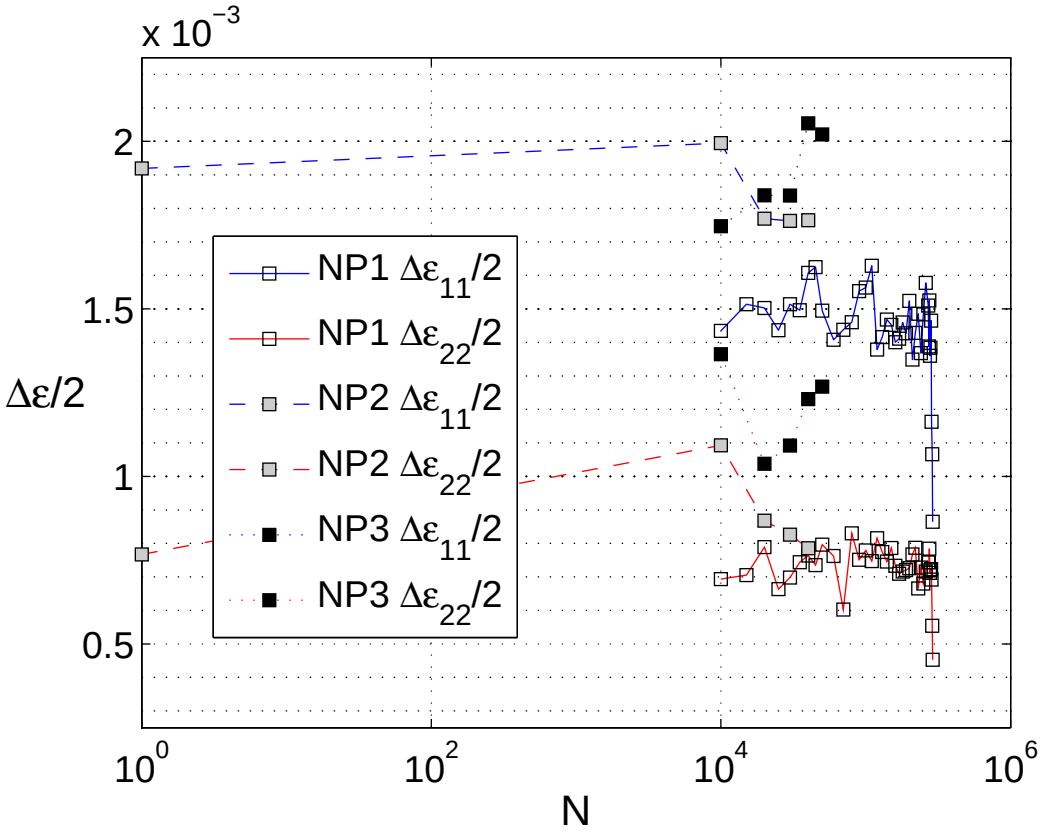
x 10^−3
2
1.5
1
0.5
Δε/2
NP1 Δε11/2
NP1 Δε22/2
NP2 Δε11/2
NP2 Δε22/2
NP3 Δε11/2
NP3 Δε22/2
10^0
10^2
10^4
10^6
N